

A Catalog of *Chandra* X-ray Sources in the Carina Nebula

Patrick S. Broos¹, Leisa K. Townsley¹, Eric D. Feigelson¹, Konstantin V. Getman¹, Gordon P. Garmire¹, Thomas Preibisch², Nathan Smith³, Brian L. Babler⁴, Simon Hodgkin⁵, Rémy Indebetouw⁶, Mike Irwin⁵, Robert R. King⁷, Jim Lewis⁵, Steven R. Majewski⁶, Mark J. McCaughrean^{7,8}, Marilyn R Meade⁴, Hans Zinnecker⁹

patb@astro.psu.edu

ABSTRACT

We present a catalog of $\sim 14,000$ X-ray sources observed by the ACIS instrument on the *Chandra X-ray Observatory* within a 1.42 square degree survey of the Great Nebula in Carina, known as the *Chandra* Carina Complex Project (CCCP). This study appears in a Special Issue of the ApJS devoted to the CCCP. Here, we describe the data reduction and analysis procedures performed on the X-ray observations, including calibration and cleaning of the X-ray event data, point source detection, and source extraction. **The catalog appears to be complete across most of the field to an absorption-corrected total-band luminosity of $\sim 10^{30.7}$ erg s⁻¹ for a typical low-mass pre-main sequence star.** Counterparts to the X-ray sources are identified in a variety of visual, near-infrared, and mid-infrared surveys. The X-ray and infrared source properties presented here form the basis of many CCCP studies of the young stellar populations in Carina.

Subject headings: ISM: individual objects (Carina Nebula) — open clusters and associations: individual (Tr14, Tr15, Tr16) — stars: formation — stars: pre-main sequence — X-Rays: stars

1. INTRODUCTION

The *Chandra* Carina Complex Project (CCCP) is a 1.42 square degree survey of the Great Nebula in Carina with the Imaging array of the Advanced CCD Imaging Spectrometer (ACIS-I, Garmire et al. 2003) on the *Chandra X-ray Observatory*. Townsley et al. (2011a) discuss the survey motivation and design, provide an observing log for the ACIS observations, and present several figures that place the footprint of the survey in an astronomical context. That work and the material presented here initiate a Special Issue of the ApJS devoted to the CCCP.

We describe here the data reduction and analysis procedures underlying various data products that are widely used by the remaining studies in this series. Section 2 discusses the calibration and cleaning of the X-ray event data, point source detection, and source extraction. Properties of the resulting X-ray point sources are presented in Section 3. Visual and infrared (IR) counterparts to the X-ray sources are reported in Section 4, and the reliability of the counterpart identification is discussed in Section 5. Section 6 discusses the completeness and reliability of the X-ray catalog.

2. DATA REDUCTION AND EXTRACTION METHODS

The CCCP survey consists of 38 ACIS-I observations totaling 1.2 Ms organized into 22 pointings (Townsley et al. 2011a, Table 1 and Figure 4). *Chandra* surveys of similar complexity include a ~ 2 Ms observation of the

¹Department of Astronomy & Astrophysics, 525 Davey Laboratory, Pennsylvania State University, University Park, PA 16802, USA

²Universitäts-Sternwarte, Ludwig-Maximilians-Universität, Scheinerstr. 1, 81679 München, Germany

³Steward Observatory, University of Arizona, 933 North Cherry Avenue, Tucson, AZ 85721, USA

⁴University of Wisconsin Department of Astronomy, 475 N. Charter St., Madison, WI 53706, USA

⁵Cambridge Astronomical Survey Unit, Institute of Astronomy, Madingley Road, Cambridge, CB3, UK

⁶Department of Astronomy, University of Virginia, P. O. Box 400325, Charlottesville, VA 22904-4325, USA

⁷Astrophysics Group, College of Engineering, Mathematics, and Physical Sciences, University of Exeter, Exeter EX4 4QL, UK

⁸European Space Agency, Research & Scientific Support Department, ESTEC, Postbus 299, 2200 AG Noordwijk, The Netherlands

⁹Astrophysikalisches Institut Potsdam, An der Sternwarte 16, 14482 Potsdam, Germany

Galactic Center region (Muno et al. 2009), the CHAMP survey of 130 extragalactic fields (Kim et al. 2007), the ~ 1.8 Ms observation of the extragalactic C-COSMOS region (Puccetti et al. 2009), and a ~ 2 Ms observation of the extragalactic CDF-S field (Luo et al. 2008).

Our data analysis techniques are discussed at length by Broos et al. (2010), hereafter referred to as B10; we briefly review the procedure here. *Chandra*-ACIS event data are calibrated and cleaned as described in Section 3 of B10. Those procedures seek to improve the accuracy of event properties (individual event positions, alignment of the *Chandra* coordinate system to an astrometric reference, energy calibration) and seek to discard events that are likely caused by various instrumental background components. A cosmic ray artifact known as “afterglow”¹ creates a particularly troublesome type of background—a group of events appearing at nearly the same location on the detector in nearly consecutive CCD frames. Since no single currently-available method for identifying afterglow events is appropriate for both weak and bright sources, we adopt a bifurcated workflow in which heavily-cleaned data are used for source detection and lightly-cleaned data are used for source extraction (see B10, Section 3 and Figure 1).

Data from two detectors lying far off-axis in the ACIS S-array, available for most observations, were calibrated and cleaned as above. However, S-array data were not used for source detection and were not routinely extracted, due to the very poor angular resolution of the *Chandra* mirrors at large off-axis angles. In a few cases, very bright sources produced S-array data that were very useful for studies of individual stars (Townsend et al. 2011a; Parkin et al. 2011).

Candidate point sources are identified in each of the CCCP pointings individually using two methods (see B10, Section 4.2). First, twelve images (energy bands 0.5–2 keV, 2–7 keV, 0.5–7 keV in combination with four pixel sizes) are searched by the standard *Chandra* detection tool, *wavdetect*² (Freeman et al. 2002). Second, **Lucy-Richardson image reconstruction (Lucy 1974) is performed on overlapping images (0.5–8 keV) that tile each CCCP pointing, sized ($1.5' \times 1.5'$) so that the *Chandra* PSF is relatively constant within each tile; peaks in the reconstructed tiles are adopted as candidate sources.** Candidate sources are *not* obtained from observations in other bands (e.g., visual or IR).

These candidate sources are extracted from all the observations in which they appear on the ACIS I-array using the *ACIS Extract*³ (*AE*) package (see B10, Section 5). Sixty percent of CCCP sources were observed multiple (2–7) times, as illustrated by the CCCP exposure map, which is shown in Figure 8 here, Figure 4 in Townsend et al. (2011a), and Figure 2 in B10. The range of off-axis angles, and thus the range of extraction aperture sizes, found among the multiple observations of a single source is often small—when observations share the same pointing or when observations barely overlap—but can be large when observations moderately overlap.

The positions of source candidates are updated with *AE* estimates, using a subset of each source’s extractions chosen to minimize the position uncertainty (see B10, Section 6.2 and 7.1). A source significance statistic is calculated with respect to the local background level (see B10, Section 4.3), using a subset of each source’s extractions chosen to maximize that significance (see B10, Section 6.2). This **decision** to ignore some observations of a source effectively prevents the very poor point spread function (PSF) of an off-axis observation from spoiling the detection or position estimate of a source that was also observed with a very good PSF on-axis. As the Carina field has bright astrophysical diffuse emission with complex structure, the use of a local rather than global background source existence criterion is important. Only candidates found to be significant are accepted as X-ray sources; expressed in terms of source properties reported in Table 1, **a detection requires both `SrcCounts.t` ≥ 3 and `ProbNoSrc.min` < 0.01 .** Iterative pruning of source candidates and re-extraction continues until no candidates are found to be insignificant (see B10, Section 4.1). **Our selection of the `ProbNoSrc.min` threshold is discussed further in Section 6.2.**

Photometry, spectra, light curves, and a variety of apparent source properties (Section 3) are derived for sources in the final catalog, using a subset of each source’s extractions chosen to balance the conflicting goals of minimizing photometric uncertainty and of avoiding photometric bias (see B10, Section 6.2).

The CCCP survey region includes several rich young stellar clusters, and some sparse but compact stellar groups,

¹<http://cxc.harvard.edu/ciao/why/afterglow.html>

²http://asc.harvard.edu/ciao/download/doc/detect_manual

³http://www.astro.psu.edu/xray/acis/acis_analysis.html

where source crowding can be important. In such cases, the source detection is largely based on the maximum likelihood image reconstruction where the blurring effects of the PSF are reduced. Photons are then extracted in apertures based on the local PSF shape but reduced in size to avoid overlap with adjacent source extraction regions. While the procedures are well-established in B10 with little subjective judgment involved, it is important to recognize that the source identifications and extractions in very crowded regions represent only one plausible interpretation of the data.

The *Chandra* data analysis system, *CIAO*, (Fruscione et al. 2006), the *SAOImage ds9* visualization tool (Joye & Mandel 2003), and the *Interactive Data Language*⁴ (IDL) are used throughout our data analysis workflow, from data preparation through science analysis. The CCCP data were reduced with *CIAO* version 4.0.2, using CALDB version 3.4.2 for event processing and CALDB version 4.1.1 for construction of calibration data products. Models of the *Chandra*-ACIS PSF were constructed (see B10, Appendix C) using version 4.3 of the *MARX* mirror simulator⁵.

3. APPARENT X-RAY POINT SOURCE PROPERTIES

A total of 14,369⁶ point sources were identified and extracted. The CCCP observations are not appropriate for studying the luminous blue variable η Carinae, and it is omitted from our catalog even though it is a strong X-ray source; Townsley et al. (2011a) provide references to more suitable observations of this remarkable star. The CCCP catalog is depicted in Townsley et al. (2011a, Figure 3 and 4), and in Broos et al. (2011, Figure 4). No single figure can adequately represent such a wide (1.4 square degrees) *Chandra* field since sources as close as $<1''$ separation can be detected. However, the electronic versions of those figures can reveal, when zoomed, detail not visible in most printed versions.

Estimates for many apparent (not corrected for absorption) properties of the X-ray sources (see B10, Section 7) are provided in a table published electronically and available at Vizier (Ochsenbein et al. 2000). Since the table has many columns, a stub cannot be conveniently shown in print. Instead, column names that are appropriate for Vizier and column descriptions are listed in Table 1. The suffixes “_t”, “_s”, and “_h” on names of photometric quantities designate the *total* (0.5–8 keV), *soft* (0.5–2 keV), and *hard* (2–8 keV) energy bands. The SrcCounts and NetCounts quantities characterize the extraction; correction for finite extraction apertures is applied to the ancillary reference file (ARF) calibration products (see B10, Section 5.3). Thus, the lowest-level calibrated photometric quantity that can be used to compare sources would be apparent *photon* flux (see B10, Section 7.4)

$$F_{\text{photon}} \doteq \text{NetCounts} / \text{MeanEffectiveArea} / \text{ExposureTimeNominal} \quad (1)$$

which has units of photon $\text{cm}^{-2} \text{s}^{-1}$. Rough, model-independent estimates for apparent *energy* flux are provided as

$$\text{EnergyFlux} \doteq 1.602 \times 10^{-9} \text{ MedianEnergy} \times F_{\text{photon}} \quad (2)$$

in units of $\text{erg cm}^{-2} \text{s}^{-1}$, where the constant 1.602×10^{-9} arises from the conversion between keV and erg (Getman et al. 2010). Table notes provide additional information regarding the definition of source properties. Model-dependent estimates for absorption and intrinsic energy flux are provided by Broos et al. (2011, Table 8) for sources that are likely to be low-mass young stars in the Carina complex.

⁴<http://www.ittvis.com/idl>

⁵<http://space.mit.edu/cxc/marx/>

⁶ The catalog used in other CCCP studies contains 14,368 sources; one additional source (the last reported in Table 1) was identified too late in the data analysis process to be included in those studies.

– 4 –
Table 1. CCCP X-ray Sources and Properties

Column Label	Units	Description
Name	...	IAU source name; prefix is CXOGNC J (<i>Chandra X-ray Observatory</i> Great Nebula in Carina)
Label ^a	...	source name used within the CCCP project
RAdeg	deg	right ascension (J2000)
DEdeg	deg	declination (J2000)
PosErr	arcsec	1- σ error circle around (RAdeg, DEdeg)
PosType	...	algorithm used to estimate position (B10, Section 7.1)
ProbNoSrc_min	...	smallest of ProbNoSrc_t, ProbNoSrc_s, ProbNoSrc_h
ProbNoSrc_t	...	p-value ^b for no-source hypothesis (B10, Section 4.3)
ProbNoSrc_s	...	p-value for no-source hypothesis
ProbNoSrc_h	...	p-value for no-source hypothesis
ProbKS_single ^c	...	smallest p-value for the one-sample Kolmogorov-Smirnov statistic under the no-variability null hypothesis within a single-observation
ProbKS_merge ^c	...	smallest p-value for the one-sample Kolmogorov-Smirnov statistic under the no-variability null hypothesis over merged observations
ExposureTimeNominal	s	total exposure time in merged observations
ExposureFraction ^d	...	fraction of ExposureTimeNominal that source was observed
NumObservations	...	total number of observations extracted
NumMerged	...	number of observations merged to estimate photometry properties
MergeBias	...	fraction of exposure discarded in merge
Theta.Lo	arcmin	smallest off-axis angle for merged observations
Theta	arcmin	average off-axis angle for merged observations
Theta.Hi	arcmin	largest off-axis angle for merged observations
PsfFraction	...	average PSF fraction (at 1.5 keV) for merged observations
SrcArea	(0.492 arcsec) ²	average aperture area for merged observations
AfterglowFraction ^e	...	suspected afterglow fraction
SrcCounts_t	count	observed counts in merged apertures
SrcCounts_s	count	observed counts in merged apertures
SrcCounts_h	count	observed counts in merged apertures
BkgScaling	...	scaling of the background extraction (B10, Section 5.4)
BkgCounts_t	count	observed counts in merged background regions
BkgCounts_s	count	observed counts in merged background regions
BkgCounts_h	count	observed counts in merged background regions
NetCounts_t	count	net counts in merged apertures
NetCounts_s	count	net counts in merged apertures
NetCounts_h	count	net counts in merged apertures
MeanEffectiveArea_t ^f	cm ² count photon ⁻¹	mean ARF value
MeanEffectiveArea_s	cm ² count photon ⁻¹	mean ARF value
MeanEffectiveArea_h	cm ² count photon ⁻¹	mean ARF value
MedianEnergy_t ^g	keV	median energy, observed spectrum
MedianEnergy_s	keV	median energy, observed spectrum
MedianEnergy_h	keV	median energy, observed spectrum
EnergyFlux_t	erg cm ⁻² s ⁻¹	max(EnergyFlux_s, 0) + max(EnergyFlux_h, 0)
EnergyFlux_s	erg cm ⁻² s ⁻¹	See Eqn. 2.
EnergyFlux_h	erg cm ⁻² s ⁻¹	See Eqn. 2.
NetCounts.Lo.t ^h	count	1-sigma lower bound on NetCounts_t
NetCounts.Hi.t	count	1-sigma upper bound on NetCounts_t
NetCounts.Lo.s	count	1-sigma lower bound on NetCounts_s
NetCounts.Hi.s	count	1-sigma upper bound on NetCounts_s
NetCounts.Lo.h	count	1-sigma lower bound on NetCounts_h
NetCounts.Hi.h	count	1-sigma upper bound on NetCounts_h

Note. — Column labels are shown as they appear in Vizier, where formatted labels are not possible.

Note. — The first 14,368 sources—the catalog used in other CCCP studies—are sorted by RA; the 14,369th source was identified too late in the data analysis process to be conveniently inserted at its rightful position in the table.

Note. — The suffixes “_t”, “_s”, and “_h” on names of photometric quantities designate the *total* (0.5–8 keV), *soft*

(0.5–2 keV), and *hard* (2–8 keV) energy bands.

Note. — Source significance quantities (ProbNoSrc_t, ProbNoSrc_s, ProbNoSrc_h, ProbNoSrc_min) are computed using a subset of each source’s extractions chosen to maximize significance (B10, Section 6.2). Source position quantities (RAdeg, DEdeg, PosErr) are computed using a subset of each source’s extractions chosen to minimize the position uncertainty (B10, Section 6.2 and 7.1). All other quantities are computed using a subset of each source’s extractions chosen to balance the conflicting goals of minimizing photometric uncertainty and of avoiding photometric bias (B10, Section 6.2 and 7).

^aSource labels identify a CCCP pointing (Townsend et al. 2011a, Table 1); they do not convey membership in astrophysical clusters.

^bIn statistical hypothesis testing, the p-value is the probability of obtaining a test statistic at least as extreme as the one that was actually observed when the null hypothesis is true.

^cSee B10, Section 7.6 for a description of the variability metrics, and caveats regarding possible spurious indications of variability using the ProbKS_merge metric.

^dDue to dithering over inactive portions of the focal plane, a *Chandra* source is often not observed during some fraction of the nominal exposure time. (See <http://cxc.harvard.edu/ciao/why/dither.html>.) The reported quantity is FRACEXPO produced by the *CIAO* tool *mkarf*.

^eSince the extracted event data are lightly-cleaned to avoid removing legitimate X-ray events from bright sources (B10, Section 3), some background events arising from an effect known as “afterglow” (<http://cxc.harvard.edu/ciao/why/afterglow.html>) will remain. We attempt to identify afterglow events using the tool *ae_afterglow_report* (see the *AE* manual), and report the fraction of extracted events attributed to afterglow.

^fThe ancillary response file (ARF) in ACIS data analysis represent both the effective area of the observatory and the fraction of the observation for which data were actually collected for the source (ExposureFraction).

^gMedianEnergy is the *AE* quantity ENERG_PCT50-OBSERVED, the median energy of extracted events, corrected for background (B10, Section 7.3).

^hConfidence intervals (68%) for NetCounts quantities are estimated by the *CIAO* tool *aprates* (<http://asc.harvard.edu/ciao/ahelp/aprates.html>).

High-quality spectra are available for relatively few CCCP sources. Table 2 shows the number of CCCP sources that have spectra with various levels of quality (characterized by ranges of net counts in the total band, NetCounts.t); the tallies are reported separately for a set of very significant “primary” sources, defined as having a low probability of being a spurious source (ProbNoSrc_min in Table 1 less than 0.003) and the complementary set of less significant “tentative” sources ($0.003 < \text{ProbNoSrc_min} < 0.01$).

The 40 sources with the highest-quality spectra (more than 500 net counts) are listed in Table 3. Most are known or candidate OB stars that are discussed in other CCCP studies (Nazé et al. 2011; Povich et al. 2011a; Parkin et al. 2011). The three known Wolf-Rayet stars in Carina (WR 25, WR 24, WR 22) are discussed by Townsley et al. (2011a). The neutron star 104608.71-594306.4 (E1.85) is discussed by Hamaguchi et al. (2009). The 12 remaining sources in the table exhibit the time variability and high-temperature spectra (shown in Figure 1) characteristic of pre-main sequence stars during flares attributed to magnetic connection events; their inferred time-averaged intrinsic luminosities range from $\sim 10^{31.6}$ erg s $^{-1}$ to $\sim 10^{32.4}$ erg s $^{-1}$ in the total-band (0.5–8 keV).

Photon-counting detectors, such as ACIS, can suffer from a non-linearity known as *photon pile-up*⁷ when multiple X-ray photons arrive with a separation in time and space that is too small to allow each to be detected as a separate X-ray event. Pile-up effects include photometric and spectroscopic miscalibration of the observation. Total-band photometry is underestimated, because multiple photons interact to produce only one or zero events. The shape of the detected X-ray spectrum is hardened, because the energy assigned to a piled event will represent that from multiple photons.

AE screens all point source extractions for photon pile-up by estimating the observed count rate falling on an event detection cell of size 3x3 ACIS pixels, centered on the source position. Pile-up was confirmed and quantified for the at-risk extractions so identified, using an experimental Monte Carlo forward-modeling approach that reconstructs a pile-up free ACIS spectrum from a piled ACIS observation. Appendix A describes this method and illustrates its application to CCCP sources. Table 4 lists extractions of CCCP sources—all known massive stars—that were confirmed to have significant pile-up using this method.⁸ Column (6) reports the ratio of the pile-up free to observed (piled) count rate in the total (0.5–8 keV) energy band.⁹ For these piled sources, Table 1 reports total-band photometry (columns SrcCounts.t and NetCounts.t) as observed, (without correction) and all other quantities that are affected by pile-up are omitted.

⁷http://cxc.harvard.edu/ciao/why/pileup_intro.html

⁸Although source 104544.13-592428.1=C4.2144=HD 93403 had a very high event rate (0.17 count s $^{-1}$), reconstruction of the spectrum indicated very little pile-up (a value of 1.02 in column 7 of Table 1) because the source was observed very far off-axis (8') and thus had only a modest event rate per detection cell.

⁹ We choose not to use the terms “pile-up fraction” or “pile-up percentage” because the ACIS community has several conflicting definitions for those terms; see Section 1.2 in The *Chandra* ABC Guide to Pileup (http://cxc.harvard.edu/ciao/download/doc/pileup_abc.pdf).

Table 2. Quality of Spectra for CCCP Sources

NetCounts.t (count) (1)	Number of sources	
	Primary (2)	Tentative (3)
<10	6852	1424
10– 50	4934	70
50– 100	677	0
100– 500	371	0
500–1000	24	0
>1000	16	0

Table 3. CCCP sources with >500 net counts in I-array extractions

CXOGNC J ^b	Label ^a	NetCounts_t (count)	Name	SpType	CCCP citation
(1)	(2)	(3)	(4)	(5)	(6)
104410.39-594311.1	CTr16.280	24609	WR 25 (HD 93162)	WN6h + OB?	(Townesley et al. 2011a)
104544.13-592428.1	C4.2144	19161	HD 93403	O5.5(f)	(Nazé et al. 2011)
104445.04-593354.6	CTr14.3535	9274	HD 93250	O3.5V((f+))	(Nazé et al. 2011)
104422.91-595935.9	C2.1111	4169	QZ Car (HD 93206)	O9.5I	(Parkin et al. 2011)
104357.47-593251.3	CTr14.1925	2977	HD 93129A	O2If*	(Nazé et al. 2011)
104352.25-600704.0	C2.547	2564	WR 24 (HD 93131)	WN6-A	(Townesley et al. 2011a)
104508.23-594607.0	CTr16.3102	1909	Cl* Trumpler 16 MJ 496	O8.5V	(Nazé et al. 2011)
103909.94-594714.5	SB2.6	1864		candidate OB star	(Povich et al. 2011a)
104505.90-594006.0	CTr16.2805	1653	HD 303308	O4V((f+))	(Nazé et al. 2011)
104752.54-600215.2	C5.1260	1573			Figure 1
104456.27-593830.4	CTr16.1450	1458			Figure 1
104433.74-594415.4	CTr16.749	1408	HD 93205	O3.5V((f+)) + O8V	(Nazé et al. 2011)
104246.53-601207.0	SP2.103	1403		candidate OB star	(Povich et al. 2011a)
104402.75-593946.0	CTr16.172	1278		candidate OB star	(Povich et al. 2011a)
104154.91-594123.6	C1.99	1249		candidate OB star	(Povich et al. 2011a)
104815.18-594319.7	E4.67	1084			Figure 1
104243.76-593954.2	C1.549	976			Figure 1
104441.80-594656.4	CTr16.1028	976	Cl Trumpler 16 100	O5.5V	(Nazé et al. 2011)
104055.32-594239.7	SB1.81	955			Figure 1
104417.54-595350.5	C2.995	822			Figure 1
104436.23-600529.0	C2.1238	820	HD 93222	O8III((f))	(Nazé et al. 2011)
104356.16-593250.9	CTr14.1731	716			Figure 1
104357.65-593253.7	CTr14.1963	685	HD 93129B	O3.5V((f+))	(Nazé et al. 2011)
104609.90-602635.5	SP4.114	680			Figure 1
104837.74-601325.7	SP3.222	668	LS 1932 (HD 93843)	O5V	(Nazé et al. 2011)
104117.50-594037.0	SB1.176	664	WR 22 (HD 92740)	WN7-A	(Townesley et al. 2011a)
104516.52-594337.1	CTr16.3341	624	Cl Trumpler 16 112	O5.5/6V((f+?p)) + B2III/V	(Nazé et al. 2011)
104512.86-594942.3	CTr16.3272	619			Figure 1
104455.79-595826.9	C3.210	618			Figure 1
104343.29-602309.5	SP2.528	600			Figure 1
104457.51-595429.5	C3.225	574		candidate OB star	(Povich et al. 2011a)
104605.70-595049.5	E1.74	544	LS 1886 (HD 305525)	O4V	(Nazé et al. 2011)
104615.77-592728.0	C6.759	529			Figure 1
104408.84-593434.4	CTr14.2688	522	HD 93161a	O8V + O9V	(Nazé et al. 2011)
104608.71-594306.4	E1.85	522			(Hamaguchi et al. 2009)
104354.40-593257.4	CTr14.1506	519	HD 93128	O3.5V((f+))	(Nazé et al. 2011)
104220.83-590908.6	C7.58	511		candidate OB star	(Povich et al. 2011a)
104712.63-600550.8	C5.846	502	HD 93632	O5III(f)	(Nazé et al. 2011)
104557.13-595643.1	C3.1477	500	Hen 3- 485	em	(Gagné et al. 2011)

^aSource labels identify a CCCP pointing (Townesley et al. 2011a, Table 1); they do not convey membership in astrophysical clusters.

^bIAU source name; prefix is CXOGNC J (*Chandra X-ray Observatory* Great Nebula in Carina)

Table 4. Sources exhibiting photon pile-up

CXOGNC J	Label	Name	Observation	θ (')	Psffraction	Correction
(1)	(2)	(3)	(4)	(5)	(6)	(7)
104357.47-593251.3	CTr14.1925	HD 93129A	4495	0.3	0.61	1.27
104410.39-594311.1	CTr16.280	WR 25 (HD 93162)	6402	4.8	0.90	1.25
104433.74-594415.4	CTr16.749	HD 93205	6402	1.8	0.50	1.16
104422.91-595935.9	C2.1111	QZ Car (HD 93206)	9482	3.4	0.90	1.11
104445.04-593354.6	CTr14.3535	HD 93250	4495	6.3	0.89	1.05

Note. — Col. (1): IAU designation (*Name* in Table 1)
Col. (2): Source name used within the CCCP project (*Label* in Table 1)
Col. (3): Object common name
Col. (4): Observation ID
Col. (5): Off-axis angle (*Theta* in Table 1)
Col. (6): Fraction of the PSF (at 1.497 keV) enclosed within the extraction region (*Psffraction* in Table 1). A reduced PSF fraction (significantly below 90%) indicates that the source is in a crowded region.
Col. (7): Estimated ratio of pile-up free to observed (piled) count rates in the 0.5–8 keV energy band.

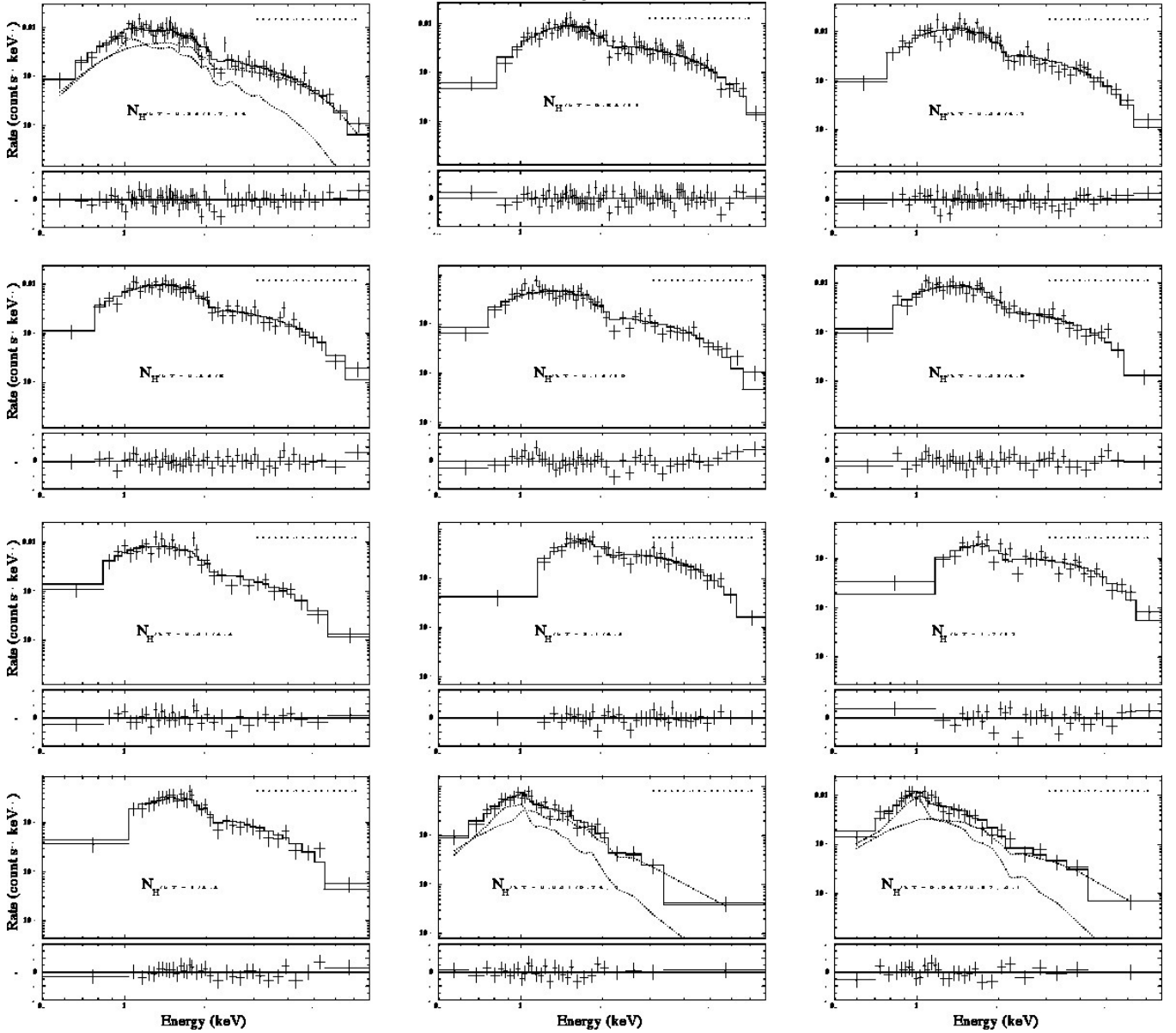


Fig. 1.— High-quality spectra for sources from Table 3 expected to be pre-main sequence stars. The spectra are modeled as one-temperature or two-temperature thermal plasmas with abundances frozen at the values adopted by the XEST study (Güdel et al. 2007), relative to Anders & Grevesse (1989), scaled to Wilms et al. (2000), using the *tbabs* absorption code. The model is implemented in *XSPEC* as *tbabs*(apec)* or *tbabs*(apec+apec)*. Column density and plasma temperatures are shown on each panel in units of 10^{22} cm^{-2} and keV.

4. COUNTERPARTS TO X-RAY POINT SOURCES

Many studies in this Special Issue rely on counterparts to CCCP sources observed in other bands. Broos et al. (2011) assign to each source a probability of Carina membership based in part on near- and mid-infrared photometry and on visual spectroscopy. CCCP studies of massive stars rely on visual spectroscopy for conclusive identification (Gagné et al. 2011; Nazé et al. 2011; Parkin et al. 2011) and on visual or infrared photometry to identify candidates (Evans et al. 2011; Povich et al. 2011a). Both X-ray and infrared data are essential to studies of pre-main sequence stars (Preibisch et al. 2011; Wang et al. 2011; Wolk et al. 2011).

Table 5 lists 19 counterpart catalogs that we have correlated with the CCCP source list. The Skiff, KR, PPMXL, UCAC3 (and its associated BSS), 2MASS, and *Spitzer* catalogs cover the entire CCCP field. The HAWK-I, SOFI, NACO, and Sana near-infrared catalogs cover portions of the field including the richest clusters. The CMD, DETWC, MDW, MJ, CP, and DAY visual photometry catalogs survey small fields on the major clusters. The X-ray study of Tr 16 by Albacete-Colombo et al. (2008) is discussed by Wolk et al. (2011).

The CCCP catalog was matched to counterpart catalogs one at a time using a simple algorithm, described in B10 (Section 8), in which the maximum acceptable separation between an X-ray source and a counterpart is based on the individual source position errors assuming Gaussian distributions, scaled so that $\sim 99\%$ of true associations should be identified as matches. When multiple sources in the counterpart catalog satisfy the match criterion, the closest one is adopted. The performance of the algorithm is studied in Section 5.

For each counterpart catalog in Table 5, N_{cat} gives the approximate number of catalog entries lying in the CCCP field, and N_{CCCP} gives the number of catalog entries that are successfully matched with X-ray sources. Preliminary matching runs were used to estimate and remove shifts (but not rotations) between each counterpart catalog and an appropriate astrometric reference, usually the Naval Observatory Merged Astrometric Dataset¹⁰ (NOMAD, Zacharias et al. 2004); the ACIS data have also been aligned to NOMAD. These catalog offsets are given in columns (6) and (7). Median separations among the identified counterparts are reported as r_{median} in Table 5. For most of the catalogs, $>80\%$ of the counterparts have separations less than $1''$. Figure 2 maps the CCCP sources with identified counterparts for some of the catalogs listed in Table 5.

Selected information about the identified counterparts in all the catalogs in Table 5 are reported in a single table with 14,368 rows representing the CCCP sources. The table is available in the electronic version of this paper, and at Vizier (Ochsenbein et al. 2000). Column names and descriptions are listed in Table 6. The first four columns are reproduced from Table 1 to identify each CCCP source. The Identifier, SpType, and SpRef columns provide an historical name for the source, report the spectral type we have adopted in the CCCP, and report a reference for that spectral type. These quantities are taken from Gagné et al. (2011) when available, and from Skiff (2009) otherwise.

Columns named “Offset(*)” report distances between CCCP and counterpart sources, after astrometric alignment of the catalogs. The remaining columns appear in groups corresponding to each counterpart catalog. Within each group, a column named “Id(*)” reports a unique identifier in the counterpart catalog. For the convenience of the reader,¹¹ additional columns give photometry or other information from the counterpart catalog.¹²

¹⁰<http://www.nofs.navy.mil/nomad/>

¹¹Ideally, Table 6 would report only the counterpart identifiers, and the reader would retrieve whatever set of previously published counterpart columns are desired at the time Table 6 is downloaded. However, no astronomy catalog server known to the authors can perform this “join” service.

¹²No screening of the re-published columns has been performed, e.g., removal of photometry estimates that are flagged as low quality by the original authors. Readers interested in counterpart properties for detailed studies are advised to identify CCCP sources in the original catalogs (using the “Id” entries in Table 6) and interpret that counterpart data appropriately.

Table 5. Summary of catalogs correlated with *Chandra* Carina sources

Catalog	Scope	Reference	N_{cat}	N_{CCCP}	$\Delta R.A.$	ΔDec	r_{median}
(1)	(2)	(3)	(4)	(5)	($''$) (6)	($''$) (7)	($''$) (8)
Skiff	Visual spectral types	Skiff (2009)	271	130	0.00	0.01	0.19
KR	Visual photometry	Kharchenko & Roeser (2009)	363	114	0.05	0.02	0.22
PPMXL	CCD proper motions (PMs)	Roeser et al. (2010)	30286	1006	0.00	0.00	0.41
UCAC3	CCD PMs	Zacharias et al. (2010)	23557	1471	0.00	0.00	0.33
BSS	Bright star PMs	Urban et al. (2004)	47	18	0.00	0.00	0.16
CMD	Photographic PMs, Tr 14, Tr 16, Cr 232	Cudworth et al. (1993)	577	141	0.62	0.59	0.33
DETWIC	Visual photometry, Tr 14 & 16	DeGioia-Eastwood et al. (2001)	853	237	0.53	0.16	0.27
MDW	Visual spectral types, Cr 228	Massey et al. (2001)	73 ^a	35	^a	^a	0.19
MJ	Visual photometry, Tr 14 & 16	Massey & Johnson (1993)	768	178	0.43	0.27	0.41
CP	High-mass photometry, Cr 228	Carraro & Patat (2001)	1112	27	-0.64	0.11	0.68
DAY	Low-mass photometry, Cr 228	Delgado et al. (2007)	152	17	-0.05	-0.03	0.81
HAWK-I	Deep near-infrared photometry	HAWKI-I (2009)	595148	6583	-0.01	-0.02	0.31
2MASS	Shallow near-infrared photometry	Cutri et al. (2003)	130164	6194	0.00	0.00	0.37
SOFI	Deep near-infrared photometry, Tr 14	Ascenso et al. (2007)	4739	849	0.02	0.00	0.18
NACO	Deep near-infrared photometry, Tr 14	Ascenso et al. (2007)	178	54	-0.01	-0.01	0.17
Sana	Deep near-infrared photometry, Tr 14	Sana et al. (2010)	1955	371	-0.06	0.04	0.16
SpVela	Mid-infrared photometry (<i>Spitzer</i>)	Povich et al. (2011b)	130871	6543	0.00	0.00	0.38
SpSmith	Mid-infrared photometry (<i>Spitzer</i>)	Smith et al. (2010)	97901	3811	0.00	0.00	0.44
AC	ACIS observation of Tr 16	Albacete-Colombo et al. (2008)	1035	935	0.19	-0.01	0.18

^aThe reported positions for two of the 75 MDW sources do not appear to coincide with any 2MASS source. We ignored those sources, and adopted 2MASS positions for the 73 remaining.

Table 6. Counterpart Properties

Column Label	Units	Description
Name	...	official name of X-ray source (prefix is CXOGNC J)
Label	...	X-ray source name used within the CCCP project
Offset(Skiff)	arcsec	offset from matching ACIS source
Offset(KR)	arcsec	offset from matching ACIS source
Offset(PPMXL)	arcsec	offset from matching ACIS source
Offset(UCAC3)	arcsec	offset from matching ACIS source
Offset(BSS)	arcsec	offset from matching ACIS source
Offset(CMD)	arcsec	offset from matching ACIS source
Offset(DETWC)	arcsec	offset from matching ACIS source
Offset(MDW)	arcsec	offset from matching ACIS source
Offset(MJ)	arcsec	offset from matching ACIS source
Offset(CP)	arcsec	offset from matching ACIS source
Offset(DAY)	arcsec	offset from matching ACIS source
Offset(HAWK-I)	arcsec	offset from matching ACIS source
Offset(2MASS)	arcsec	offset from matching ACIS source
Offset(SOFI)	arcsec	offset from matching ACIS source
Offset(NACO)	arcsec	offset from matching ACIS source
Offset(Sana)	arcsec	offset from matching ACIS source
Offset(SpVela)	arcsec	offset from matching ACIS source
Offset(SpSmith)	arcsec	offset from matching ACIS source
Offset(AC)	arcsec	offset from matching ACIS source
Identifier	...	historical star name
SpType	...	spectral type
SpRef	...	reference for spectral type
Id(KR)	...	row identifier (<i>recno</i> in published catalog)
Bmag(KR)	mag	B band magnitude
Vmag(KR)	mag	V band magnitude
Id(PPMXL)	...	row identifier (<i>ipix</i> in published catalog)
Id(UCAC3)	...	row identifier (<i>3UC</i> in published catalog)
Id(BSS)	...	row identifier (<i>ID</i> in published catalog)
Id(CMD)	...	row identifier (<i>recno</i> in published catalog)
Vmag(CMD)	mag	V band magnitude
B-V(CMD)	mag	B-V color
Id(DETWC)	...	row identifier (<i>RAJ2000+DEJ2000</i> in published catalog)
Vmag(DETWC)	mag	V band magnitude
U-B(DETWC)	mag	U-B color
B-V(DETWC)	mag	B-V color
Id(MDW)	...	row identifier (<i>Name</i> in published catalog)
Id(MJ)	...	row identifier (<i>Star</i> in published catalog)
Vmag(MJ)	mag	V band magnitude
U-B(MJ)	mag	U-B color
B-V(MJ)	mag	B-V color
Id(CP)	...	row identifier (<i>ID</i> in published catalog)
Umag(CP)	mag	U band magnitude
Bmag(CP)	mag	B band magnitude
Vmag(CP)	mag	V band magnitude
Rmag(CP)	mag	R band magnitude
Imag(CP)	mag	I band magnitude
Id(DAY)	...	row identifier (<i>Name</i> in published catalog)
Vmag(DAY)	mag	Johnson V magnitude
U-B(DAY)	mag	Johnson U-B colour index
B-V(DAY)	mag	Johnson B-V colour index
V-Rc(DAY)	mag	Johnson-Cousins V-Rc colour index
V-Ic(DAY)	mag	Johnson-Cousins V-Ic colour index
AV(DAY)	...	Absorption in V band
Id(HAWK-I)	...	row identifier (<i>RA+DEC</i> in published catalog)
Id(2MASS)	...	row identifier (<i>Designation</i> in published catalog)

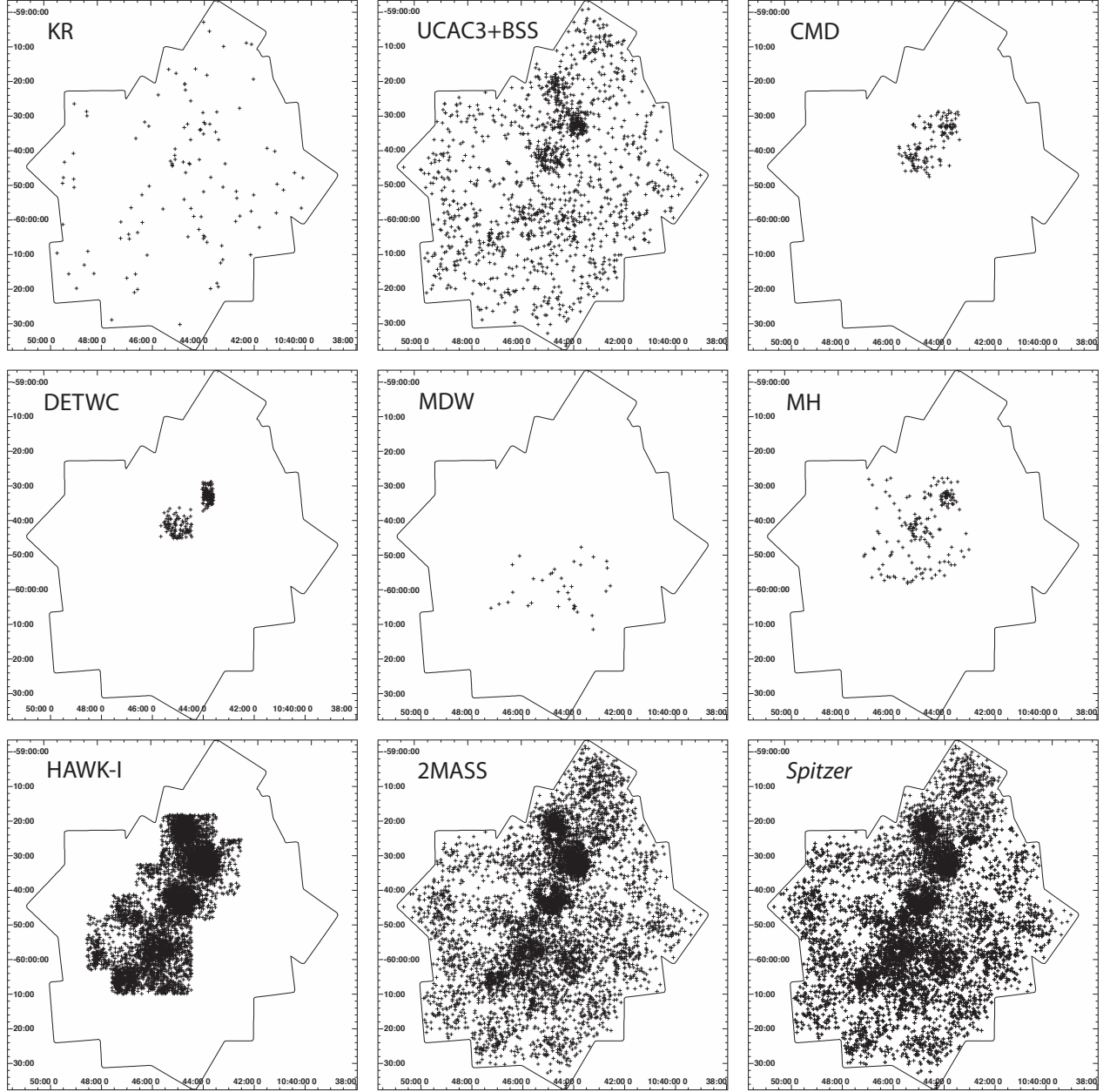


Fig. 2.— CCCP matches to selected catalogs in Table 5. The electronic version of the figure can reveal, when zoomed, detail not visible in most printed versions. Coordinates here and for all subsequent images are celestial J2000.

4.1. *Chandra* detections of Carina stars with visual spectroscopy and photometry

The General Catalog of Stellar Spectral Classifications (“Skiff” in Table 5) is an all-sky collection of stars with MK spectral types based on visual spectroscopy gathered from heterogeneous sources in the literature; 271 Skiff sources are found in the CCCP field. Gagné et al. (2011) and Nazé et al. (2011) study 200 O and B stars selected from the Skiff list; for a few of these stars we adopted positions and/or spectral types different from those reported by Skiff (2009) (Gagné et al. 2011). Three Wolf-Rayet stars in the field are discussed by Townsley et al. (2011a). Six stars with spectral types A, F, or K are assumed to lie in the foreground (Broos et al. 2011). A considerable fraction of the known OB stars in the region are not detected in the CCCP (Gagné et al. 2011) and a considerable number of likely OB members are discovered in the CCCP and do not yet have spectroscopic classifications (Povich et al. 2011a). Thus, the Skiff-CCCP counterparts can not be viewed as well-defined or complete in any criteria.

Kharchenko & Roeser (2009) (KR) provide an all-sky catalog of visual-band measurements compiled from the literature for more than 2.5 million stars brighter than $V \simeq 14$ mag; we identify 114 of these in the CCCP catalog. Massey & Johnson (1993) (MJ) and DeGioia-Eastwood et al. (2001) (DETC) are historically important *UBV* photometric surveys of the Tr 16 and Tr 14 regions. Figure 3 shows the color-magnitude diagram for the deeper DETWC survey. It shows that the CCCP X-ray survey detects a roughly constant fraction of the $18 < V < 12$ DETWC stars at all magnitudes and (moderate) absorptions, from *K* through *O* stars. It is likely that most other CCCP Carina members have similar visual photometric properties.

Two deep optical *UBVRI* photometric surveys have been made of a portion of the widely-dispersed Col 228 cluster around $10^h43^m-60^s00'$ with no strong concentration of OB stars. Carraro & Patat (2001) (CP) located 1112 stars in a ~ 20 arcmin² field, and Delgado et al. (2007) (DAY) located a larger sample in a ~ 100 arcmin² of which 152 are identified as likely pre-main sequence cluster members. Unfortunately, this location lies off-axis between two ACIS pointings where the X-ray sensitivity is reduced. Only 27 of the CP stars and 17 of the DAY stars are detected in X-rays. While small samples, they provide a glimpse at the lower mass function of the stellar population in the southwestern part of the Carina complex.

Table 6—Continued

Column Label	Units	Description
J_M(2MASS)	mag	J-band magnitude
H_M(2MASS)	mag	H-band magnitude
K_M(2MASS)	mag	Ks-band magnitude
Ph_Qual(2MASS)	...	Photometric quality flag
CC_Flg(2MASS)	...	Contamination and confusion flag
Id(SOFI)	...	row identifier (<i>recno</i> in published catalog)
Jmag(SOFI)	mag	J-band magnitude
Hmag(SOFI)	mag	H-band magnitude
Ksmag(SOFI)	mag	Ks-band magnitude
Id(NACO)	...	row identifier (<i>recno</i> in published catalog)
Jmag(NACO)	mag	J-band magnitude
Hmag(NACO)	mag	H-band magnitude
Ksmag(NACO)	mag	Ks-band magnitude
Id(Sana)	...	row identifier (<i>recno</i> in published catalog)
Hmag(Sana)	mag	H-band magnitude
Ksmag(Sana)	mag	Ks-band magnitude
Id(SpVela)	...	row identifier (<i>DESIG</i> in published catalog)
mag3.6(SpVela)	mag	3.6 μ m magnitude
mag4.5(SpVela)	mag	4.5 μ m magnitude
mag5.8(SpVela)	mag	5.8 μ m magnitude
mag8.0(SpVela)	mag	8.0 μ m magnitude
Id(SpSmith)	...	row identifier (<i>DESIG</i> in published catalog)
mag3.6(SpSmith)	mag	3.6 μ m magnitude
mag4.5(SpSmith)	mag	4.5 μ m magnitude
mag5.8(SpSmith)	mag	5.8 μ m magnitude
mag8.0(SpSmith)	mag	8.0 μ m magnitude
Id(AC)	...	row identifier (<i>CXOTr16</i> in published catalog)

4.2. Proper motion measurements of *Chandra* stars

The dense, all-sky PPMXL (Roeser et al. 2010) and UCAC3 (Zacharias et al. 2010) (with its Bright Star Supplement) proper motion surveys have counterparts to 1,006 and 1,471 CCCP sources, respectively. The Carina proper motion survey of Cudworth et al. (1993) (CMD), based on a century of photographic plates, has 141 CCCP counterparts.

In principle, proper motion measurements can help discriminate rapidly-moving foreground Galactic field stars from Carina members. For example, almost all of the PPMXL sources that are spectroscopically confirmed OB stars (Skiff 2009)—objects very likely to be Carina members—are found to lie in a small circular region of proper motion space¹³ that contains a minority (445/1006) of all PPMXL sources identified in the CCCP catalog. However, we were unable to identify a boundary in proper motion space that would select a set of CCCP sources that is clearly consistent with a foreground population, i.e., an unclustered sample with median X-ray energies indicating low interstellar absorption. This is difficult to interpret, and may reflect observational limitations in automatically measuring proper motions in nebular regions. As we find no simple interpretation to the proper motion characteristics of CCCP sources, we do not consider proper motion to be a useful measurement for classifying CCCP sources (Broos et al. 2011).

4.3. *Chandra* counterparts for near-infrared surveys

Near-infrared (*JHK*) photometry provides vital information to many CCCP studies. The ubiquitous Two Micron All Sky Survey (2MASS) offers very well calibrated positions and photometry across the entire sky, however its moderate spatial resolution and sensitivity are not adequate to detect CCCP sources that are crowded and/or faint. For the majority of CCCP sources (those in the major clusters) excellent near-IR data from the High Acuity

¹³ A circular region centered at $(\mu_\alpha, \mu_\delta) = (-6.45, +2.61)$ mas yr⁻¹ with a radius of 13 mas yr⁻¹ contains 109 of the 110 PPMXL sources that are spectroscopically confirmed OB stars.

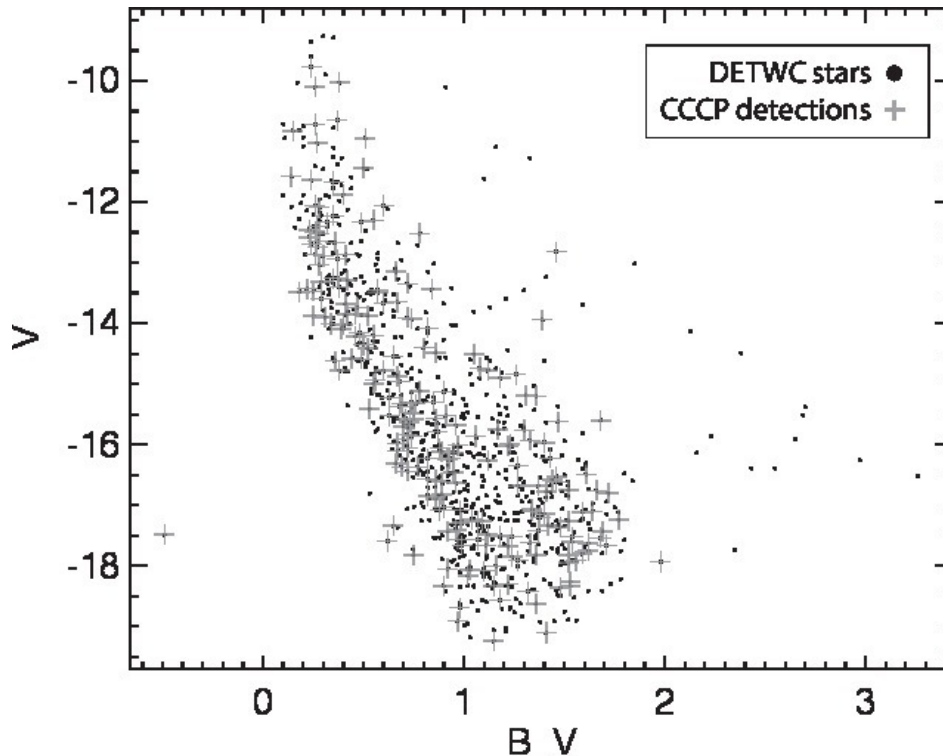


Fig. 3.— *BV* color-magnitude diagram of $V < 18$ stars around Tr 14 and Tr 16 reported by DeGioia-Eastwood et al. (2001). All DETWC sources are shown as dots; CCCP detections are shown as pluses.

Wide-field K-band Imager (HAWK-I) instrument¹⁴ (Kissler-Patig et al. 2008) was available to us; Preibisch et al. (2011) discuss these data in depth. Very high resolution, but very narrow-field, observations of the core of the Tr 14 cluster were provided by Ascenso et al. (2007) and by Sana et al. (2010).

4.4. *Chandra* counterparts for wide-field mid-infrared surveys

Photometric observations of mid-infrared (MIR) point sources are invaluable to studies of star forming regions in a number of ways. Young stellar objects are readily identified by the MIR emission of their circumstellar disks or accreting envelopes, arising from the reprocessing of stellar radiation. Strong constraints on the luminosity of OB stars can be obtained from modeling of visual (UBV) and IR spectral energy distributions (SED’s), allowing the detection of candidate massive stars and the direct measurement of visual extinction (Povich et al. 2011a). The CCCP had access to two data sets from the *Spitzer Space Telescope*: deep observations of two large fields (Spitzer Proposal ID 3420, PI N. Smith) covering the South Pillars and the western wall of the southern superbubble lobe (Smith et al. 2010), and the shallower Vela-Carina Survey (*Spitzer* Proposal ID 40791, PI S. Majewski) covering the entire field (Povich et al. 2011b).

5. RELIABILITY OF IDENTIFIED COUNTERPARTS

Any counterpart matching enterprise is forced to balance two type of failures—missed matches and spurious matches—analogous to the balance any source detection enterprise must strike between incompleteness and spurious detection. Broos et al. (2007, Appendix) describe a Monte Carlo method for estimating the performance expected from our matching procedure. The X-ray catalog is modeled as a mixture of two populations: an “associated population” for which true counterparts exist in the counterpart catalog, and an “unassociated population” for which no counterparts exist in the counterpart catalog.¹⁵ This mixture is represented by the left-hand oval in Figure 4.

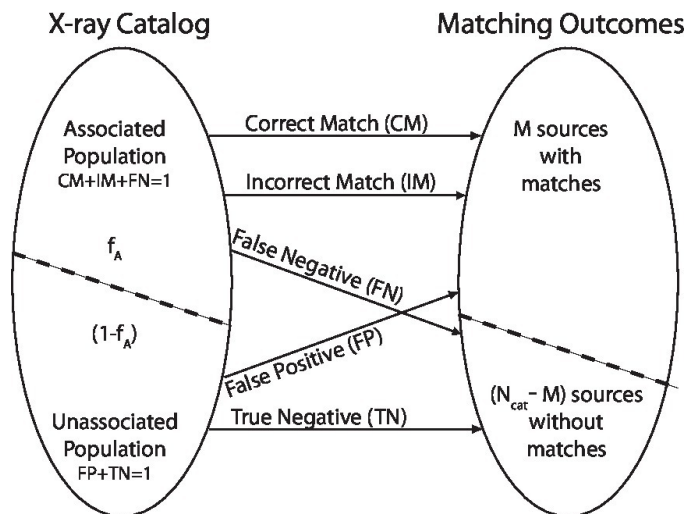


Fig. 4.— Diagram of all possible ways in which matching an X-ray catalog, comprised of two source populations (left oval), with a counterpart catalog can produce associations (upper portion of right oval) and non-associations (lower portion of right oval). Section 5 defines the outcome pathways (arrows) and their probabilities (CM, IM, FN, FP, TN), and the catalog populations (*associated* and *unassociated*).

In our Monte Carlo method, the process of matching the associated population to the counterpart catalog is simulated many times in order to estimate the frequency of three possible outcomes—correct matches (CM), incorrect

¹⁴ HAWK-I observations were obtained on the ESO 8-meter Very Large Telescope (VLT) at Paranal Observatory, Chile, under ESO programme 60.A-9284(K).

¹⁵ Some counterparts will be missing from the counterpart catalog, e.g., because they are too bright, too dim, too crowded with other sources, or lost in diffuse emission.

matches (IM), and false negatives (FN). An IM occurs when the true counterpart is identified as a plausible match, but is rejected in favor of an “interloper”—another source in the counterpart catalog that (by chance) produces a more plausible match that is mistakenly accepted. A FN is a catalogued counterpart that is in fact associated with the X-ray source, but is not identified because the observed X-ray and counterpart positions of the source are too distant to meet the match criterion. Separate simulations for the unassociated population estimate the frequency of two possible outcomes—true negatives (TN) and false positives (FP). A FP is a chance superposition of an unrelated source in the counterpart catalog and an X-ray source that has no true counterpart.

The fraction of sources in the actual X-ray catalog expected to belong to the associated population, f_A , is estimated by equating the number of actual sources for which no match was identified with the sum of our predictions for the two pathways that can produce that outcome (the FN fraction multiplied by the size of the associated population plus the TN fraction multiplied by the size of the unassociated population):

$$(N_{cat} - M) = N_{cat}[f_A \times \text{FN} + (1 - f_A) \times \text{TN}], \quad (3)$$

where N_{cat} is the number of entries in the counterpart catalog and M is the number of X-ray sources that produced matches (see Figure 4).

We have applied this method to estimate the expected outcomes for the ACIS/Sana, ACIS/2MASS, and ACIS/HAWK-I matching procedures for two complementary samples of the ACIS catalog: a set of very significant “primary” sources, defined as having a low probability of being a spurious source (ProbNoSrc_min in Table 1 less than 0.003) and a set of less significant “tentative” sources ($0.003 < \text{ProbNoSrc_min} < 0.01$). The very deep Sana catalog covers a small field on Tr 14; Figure 5 shows the very good agreement between the CCCP catalog and IR observations in this very crowded field. The deep HAWK-I catalog covers about one third of the CCCP field (Figure 2). Although the 2MASS catalog spans the entire CCCP field of view, we estimated matching outcomes over only the HAWK-I field of view to facilitate comparison with the HAWK-I results.

For the primary and tentative samples and for each counterpart catalog, Table 7 reports the total number of ACIS sources (column N_{CCCP}) in the field of view analyzed and the expected matching outcomes for those sources: correct matches (CM), incorrect matches (IM), and false negatives (FN) for the associated population; true negatives (TN) and false positives (FP) for the unassociated population.

As expected, the fraction of ACIS sources (column CM) expected to produce matches that identify *true counterparts* varies with the sensitivity of the counterpart catalog: 81% (primary) and 38% (tentative) for Sana, 74% and 23% for HAWK-I, 50% and 12% for 2MASS. Among the primary ACIS sources, the fraction of asserted matches expected to be spurious is low: 0.10 for Sana ($[6 + 3]/[81 + 6 + 3]$), 0.18 for HAWK-I ($[9 + 7]/[74 + 9 + 7]$), and 0.04 for 2MASS ($[0 + 2]/[50 + 0 + 2]$).

Table 7. Estimated outcomes of ACIS/Sana, ACIS/HAWK-I, and ACIS/2MASS matching.

CCCP Sample		Associated			Unassociated	
Reliability	N_{CCCP}	CM	IM	FN	TN	FP
(1)	(2)	(3)	(4)	(5)	(6)	(7)
Sana						
primary	380	81%	6%	1%	8%	3%
tentative	22	38%	3%	0%	36%	22%
HAWK-I						
primary	6749	74%	9%	1%	9%	7%
tentative	663	23%	5%	0%	29%	43%
2MASS in HAWK-I field						
primary	6749	50%	0%	1%	48%	2%
tentative	663	12%	0%	0%	83%	4%

Note. — Matching outcomes (Section 5) consist of correct matches (CM), incorrect matches (IM), and false negatives (FN) for the associated population; true negatives (TN) and false positives (FP) for the unassociated population.

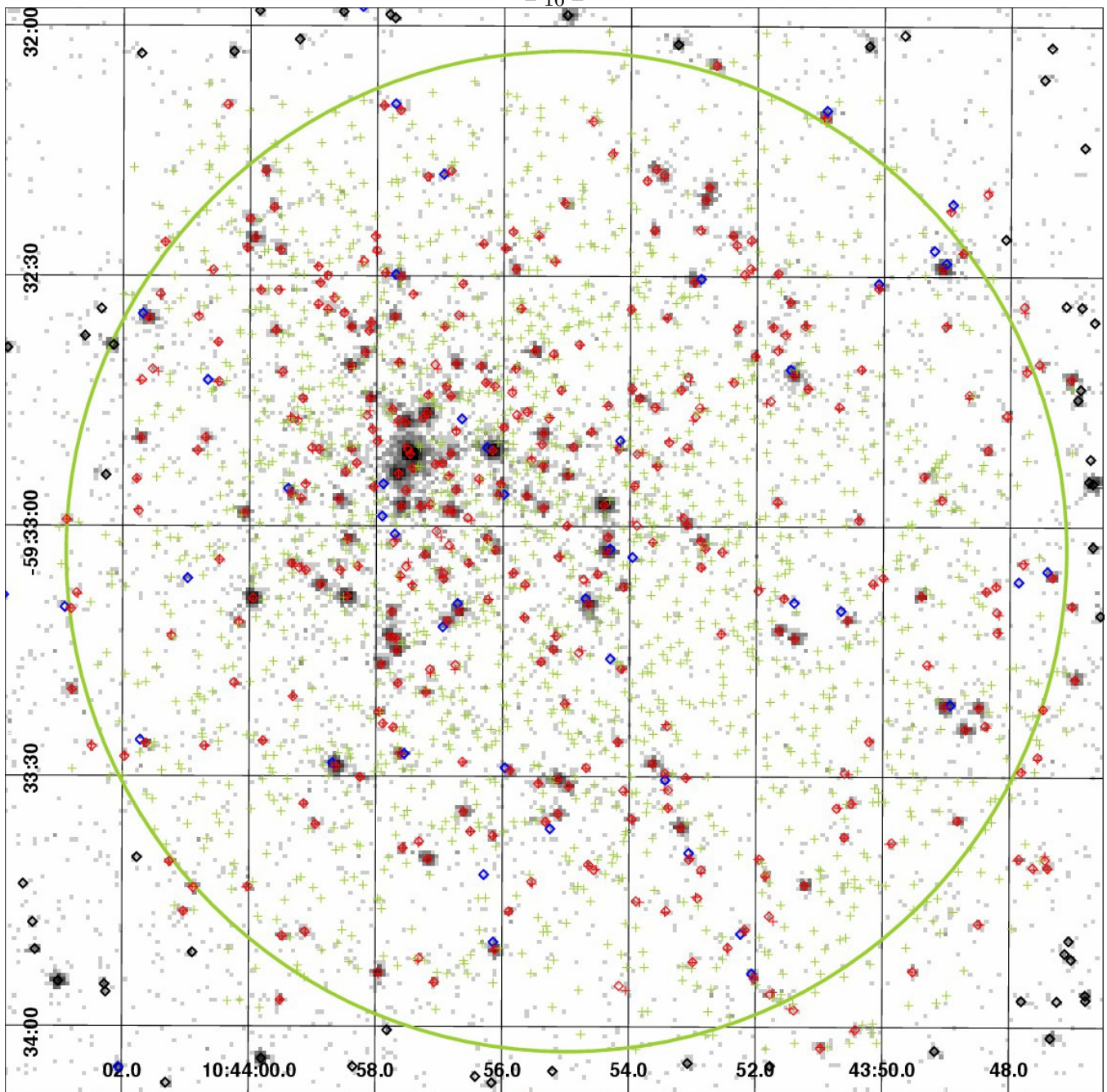


Fig. 5.— Matches identified between the CCCP (red diamonds) and a high-resolution observation of the Tr 14 core (Sana et al. 2010) (red pluses), with unmatched CCCP (blue diamonds) and Sana (green pluses) sources. CCCP sources likely to be outside the Sana field of view (green circle) are shown as black diamonds. The underlying image is the CCCP data, scaled so that pixels with a single X-ray event are light gray. The electronic version of the figure can reveal, when zoomed, detail not visible in most printed versions. **[[Note to referee and journal staff: we would like to examine proofs of this figure before deciding whether a second panel, showing a close-up of the most crowded region, should be added.]]**

Among the tentative ACIS sources, spurious matches are expected to be more common. Spurious match fractions are 0.40 for Sana ($[3+22]/[38+3+22]$), 0.68 for HAWK-I ($[5+43]/[23+5+43]$), and 0.25 for 2MASS ($[0+4]/[12+0+4]$). At least three effects can explain this result. First, the position errors assigned to the tentative ACIS sources (median $0.44''$) are larger than for the primary sources (median $0.33''$), directly increasing the “footprints” around ACIS sources in which a spurious counterpart can be identified. Second, by definition the tentative sample is expected to harbor a higher fraction of spurious ACIS detections, for which there is no true counterpart to be found. Third, since tentative sources tend to be less X-ray luminous than primary sources, if there is any correlation between X-ray and

visual/IR luminosity then tentative X-ray sources are likely to have weak visual/IR emission that is not detectable in the counterpart catalog.

The notion that the X-ray catalog can be viewed as a mixture of associated and unassociated populations—on which the matching outcome estimation method above is based—is visually demonstrated in Figure 6, where ACIS/HAWK-I separations (in arcseconds) of matching sources are shown for the two simulated populations and for the actual ACIS catalog. The upper panel shows that the tentative ACIS catalog (solid) has match separations that appear to be a mixture of the associated population (dashed) and the unassociated population (dotted). The middle panel shows the same quantities for the primary ACIS catalog; the fact that the actual ACIS/HAWK-I separations (solid) are smaller than those from the associated simulation (dashed) suggests that the adopted ACIS and/or HAWK-I position errors are over-estimated. Perhaps a more informative measure of source separation is the smallest significance threshold, a parameter to the matching algorithm (see B10, Section 8), required to assert the match. The bottom panel presents the distribution of this quantity (expressed as a multiple of σ for a Gaussian distribution) for the same catalogs and simulations as the middle panel. Separations among matches for the associated population (dashed) most commonly fall at $\sim 1\sigma$, falling off at higher separations. In contrast, the occurrence of separations in the unassociated population (dotted) increases with separation, reflecting the quadratic growth in area of annular footprints with increasing distance from the ACIS source. As in the middle panel, the actual ACIS/HAWK-I matches (solid) are generally smaller than those from the associated simulation (dashed), suggesting that the adopted ACIS and/or HAWK-I position errors are over-estimated.

6. QUALITY OF THE X-RAY CATALOG

6.1. Sensitivity to Point Sources

We find that very precise language is required to avoid miscommunication when discussing the “sensitivity” of a source catalog. Here, we restrict our use of that word to mean the general concept that, for any given observation, the probability of detecting a source depends on how “bright” it is; we do not use the word “sensitivity” to refer to any specific threshold. We use the term “completeness” to refer to the probability that members of a precisely defined parent population of point-like objects will be present in a precisely defined sample of detected sources. In contexts where the parent population under discussion is defined by some observational or astrophysical quantity, we use the term “completeness limit” to mean a lower-limit on that quantity for which nearly 100% of the parent population will be present in a specified sample. Thus, a “completeness limit” is properly stated in terms of a specific measured or inferred source property and in terms of a specific sample of detected sources.

Most studies that involve X-ray-selected sources will have to consider to what extent the analysis is affected by the finite sensitivity of the X-ray observations. Sensitivity is perhaps best studied via Monte Carlo simulations of synthetic data sets that contain artificial sources that are subjected to the same detection procedure used on the observed data. Since most studies need to characterize sensitivity in terms of an astrophysical, not an observational, quantity such as intrinsic (corrected for absorption) X-ray luminosity or stellar mass, the first simulation task is astrophysical—modeling the X-ray photons that *Chandra* should see for various astrophysical objects. This task is often quite difficult, requiring information that is not well known (e.g., the 3-D distribution of absorbing material and the 3-D distribution of sources) and/or requiring astrophysical models that are not well known (e.g., the relationship between stellar mass and X-ray luminosity).

After astrophysical models have predicted *apparent* (diminished by absorption) X-ray flux for synthetic stars, the second simulation task is instrumental—modeling the event data (including background) that would be produced, the data reduction process, and the source detection process. If the layout of a *Chandra* mosaic (exposure times and the pattern of observation overlap) is simple and the source detection procedure is simple, then apparent flux sensitivity can be studied without detailed Monte Carlo simulations; see for example Georgakakis et al. (2008) and references therein. However, for the complex data set and the complex detection procedure employed in the CCCP, adequate resources are simply not available to perform the complex simulations that would be required to map detection probabilities across the field.

Instead, we aspire to present here only an empirical description of detection completeness limits with respect to apparent photometric quantities, based on the astrophysical assumption that those quantities follow a powerlaw distribution that “rolls off” at the low-flux end due to decreasing detection probability. Our primary goal is to

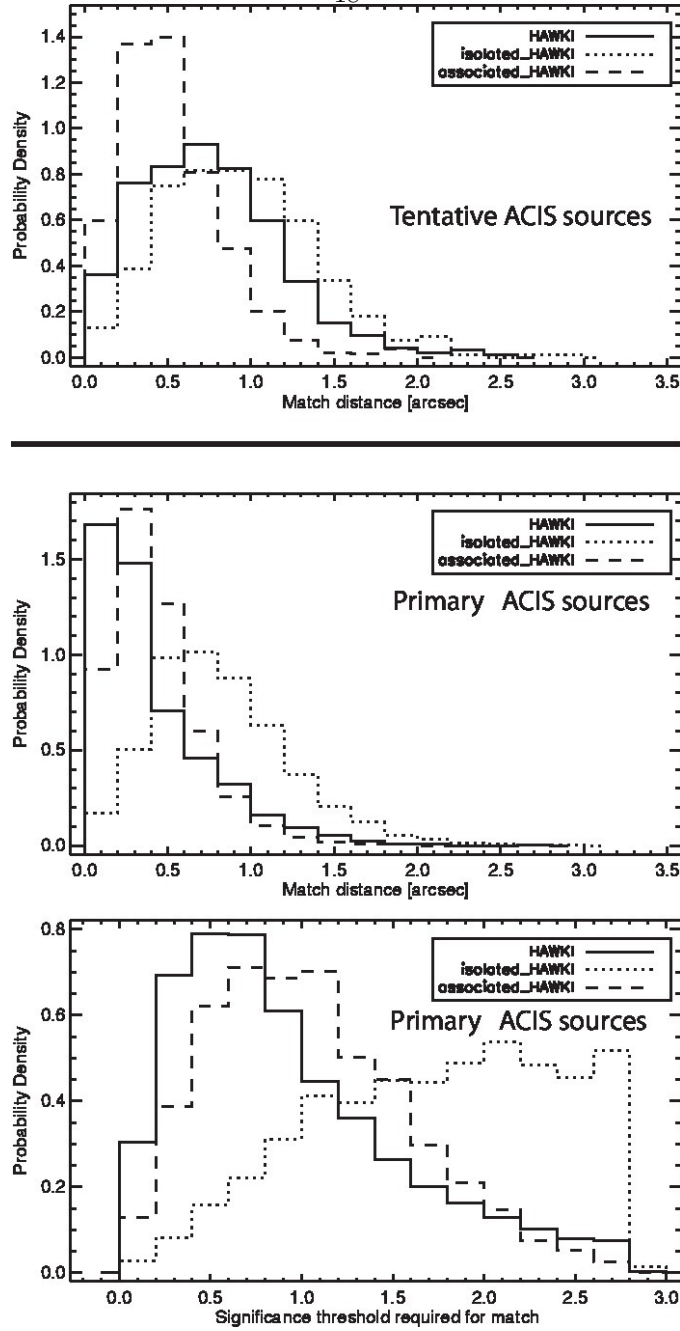


Fig. 6.— Observed separations (solid histograms) between tentative (upper panel) and primary (middle and lower panels) ACIS sources and HAWK-I counterparts, compared with simulated separations for an associated population (dashed) and an unassociated population (dotted). Separations are characterized via angular distance (upper and middle panels) and via match significance (lower panel).

visualize and quantify the large influence that off-axis angle (θ in Table 1) has on sensitivity in the CCCP catalog (and indeed in many other *Chandra* catalogs). This relationship arises from two instrumental effects. First, the extraction area, and thus any spatially-uniform background component, of a point source with a reasonable aperture (e.g., 90% PSF fraction) is ~ 100 times larger far off-axis ($\theta = 10'$) than on-axis. Second, the *Chandra* effective area far off-axis is $\sim 20\%$ lower than on-axis due to mirror vignetting.¹⁶

The upper panel of Figure 7 shows histograms of the observational quantity NetCounts.t from Table 1 (net extracted counts in the total band, 0.5–8 keV) over six disjoint ranges of off-axis angle. The source sample represented in Fig. 7 is mapped in Figure 8; we excluded 6877 sources that may exhibit intrinsic spatial variation in the luminosity

¹⁶See Figure 4.5 in the *Chandra* Proposers' Observatory Guide (http://asc.harvard.edu/proposer/POG/pog_pdf.html).

function (those lying in clusters identified by Feigelson et al. (2011)) or that have a poorly-defined off-axis angle (more than 20% variation in Theta among the covering observations).

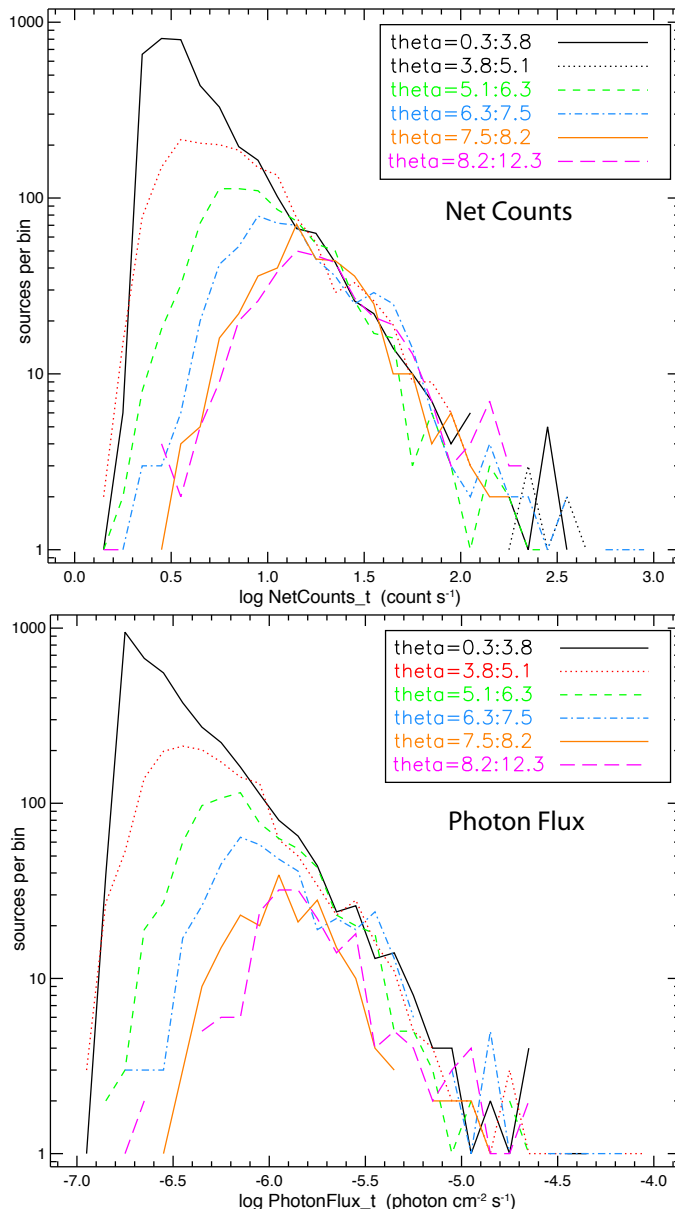


Fig. 7.— Histogram of net extracted counts (upper panel) and apparent photon flux (lower panel) for a sample of CCCP sources defined in Section 6.1, stratified by off-axis angle.

We choose to interpret the empirical distribution of NetCounts.t in each off-axis angle slice as arising from a powerlaw-distributed parent population of astrophysical sources (young stars in Carina, field stars, extragalactic objects) that has been incompletely detected at low fluxes. We performed a maximum likelihood fit of the unbinned NetCounts.t data in each slice to a powerlaw model with a low-side cutoff¹⁷, and we choose to interpret that cutoff value as the onset of incompleteness. The best-fit powerlaw exponent and the inferred completeness limit are reported as α and N_{lim} in the middle section of Table 8.

The lower panel of Figure 7 and right section of Table 8 present the same analysis carried out on a simple *calibrated* photometric quantity, an estimate of apparent (not corrected for absorption) photon flux in the total energy band (0.5–8 keV), $F_{t,\text{photon}}$ defined by Equation 1. The source sample depicted is the NetCounts.t sample,

¹⁷ Maschberger & Kroupa (2009) discuss the well-known unbiased maximum likelihood estimator for the exponent of an infinite powerlaw distribution and they propose a similar unbiased estimator for a truncated powerlaw. We have implemented these estimators using IDL in a tool called *ml_powerlaw*, which is part of our *TARA* software package (http://www.astro.psu.edu/xray/acis/acis_analysis.html).

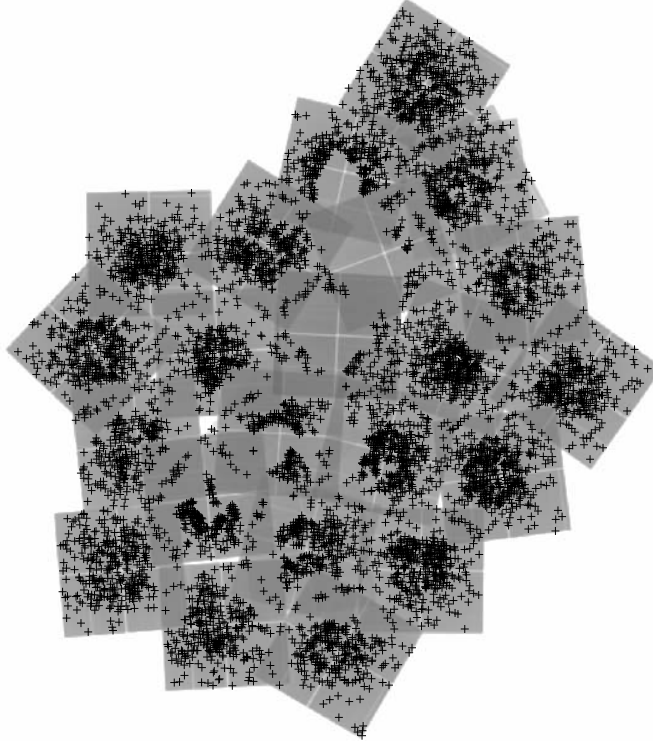


Fig. 8.— CCCP sample used in Figure 7 and to estimate completeness limits in Table 8; these are sources with well-defined off-axis angle that are not obviously associated with clusters.

less 748 sources that have off-nominal exposure time. The best-fit powerlaw exponent and the inferred photon flux completeness limit are reported as α and $F_{t,\text{photon},\text{lim}}$.

Those photon flux limits have been converted to intrinsic (corrected for absorption) luminosity limits in the total energy band (0.5–8 keV), shown as column $L_{t,c,\text{lim}}$, by making the following astrophysical assumptions. The emitting gas is modeled as the two-temperature thermal plasma that Getman et al. (2010) adopt as typical for low-mass pre-main sequence stars with moderate intrinsic luminosity, specifically the model shown in the $L_{h,c} = 10^{30.0}$ entry of their Table 1. The absorbing column is assumed to be $N_H = 0.64 \times 10^{22} \text{ cm}^{-2}$ corresponding to $A_V = 4$ mag, which Preibisch et al. (2011) find to be typical for Carina stars. The distance to Carina is assumed to be 2300

Table 8. Completeness Limits for the CCCP Catalog

Off-axis Angle		NetCounts.t (0.5–8 keV)			$F_{t,\text{photon}}$ (0.5–8 keV)			
Range (')	Median (')	N_{sample} (source)	α	$\log N_{\text{lim}}$ (count)	N_{sample} (source)	α	$\log F_{t,\text{photon},\text{lim}}$ (photon $\text{cm}^{-2} \text{ s}^{-1}$)	$\log L_{t,c,\text{lim}}$ (erg s^{-1})
(1)	(2)	(3)	(4)	(5)	(6)	(7)	(8)	(9)
0.0:3.8	2.8	3766	2.41	0.8	3651	2.29	-6.7	29.9
3.8:5.1	4.4	1613	2.38	0.9	1523	2.34	-6.2	30.4
5.1:6.3	5.7	814	2.58	1.2	749	2.34	-6.2	30.4
6.3:7.5	6.9	548	2.24	1.2	426	2.11	-6.1	30.5
7.5:8.2	7.9	387	2.40	1.2	198	2.62	-5.9	30.7
8.2:12.3	8.7	356	2.28	1.3	189	2.31	-5.9	30.7

Note. —

Col. (1): Off-axis angle range defining the sample

Col. (2): Median off-axis angle within the sample

Cols. (3) and (6): Sample size

Cols. (4) and (7): Estimated exponent of truncated powerlaw model

Cols. (5), (8), and (9): Estimated truncation threshold (completeness limit)

pc.

We wish to emphasize that the completeness limits in Table 8 are a characterization of source samples defined only by the CCCP detection process and by off-axis angle. Once a scientific study has imposed additional selection criteria—e.g., source classification, the availability of counterpart information, or the availability of individual X-ray luminosity estimates—the completeness limit for the resulting sample can be higher.

The strong variation in detection completeness with off-axis angle (~ 0.8 dex for photon flux) inferred from Table 8 is responsible for the obvious “egg-crate effect”—a greater density of sources on-axis than off-axis—seen when the full catalog is plotted on the sky, as in Figure 4 in Townsley et al. (2011a). A sensible method for suppressing this effect from any particular region on the sky (e.g., for a particular star cluster) is to trim the catalog at the photon flux limit corresponding to the largest off-axis angle included in that region. Such an approach is recommended for spatial analyses involving counting sources e.g., Feigelson et al. (2011). In that study, the “complete” sample of 3,220 Carina members is defined by $\log F_{t,\text{photon},\text{lim}} > -5.9$ photon $\text{cm}^{-2} \text{s}^{-1}$ based on the $F_{t,\text{photon},\text{lim}}$ completeness limits shown in Table 8.

However, we must emphasize that a catalog so trimmed is not expected to be complete in *other* astrophysical quantities, such as apparent X-ray luminosity (which depends on the temperature of the source) or intrinsic X-ray luminosity (which additionally depends on absorption to the source). In fact, applying a cut in NetCounts.t or PhotonFlux.t is *harmful* in such analyses because some of the discarded sources may in fact lie above the completeness limit for the quantity of interest.

Spurious sources have the potential to mask the incompleteness of legitimate detections at low fluxes, thereby biasing estimates of completeness limits. For example, in analyses like those in Section 6.1, spurious sources could “fill in” the deficit of detected legitimate sources at low fluxes in a way that obscures the departure of the detected distribution from a powerlaw model. We can roughly assess the degree to which the inferred completeness limits in Table 8 may suffer from this issue by estimating an upper limit on the fraction of sources brighter than those limits that have a reasonable risk of being spurious. For example, within the innermost off-axis angle slice ($\theta = 0\text{--}3.8'$) in Table 8, $\sim 10\%$ of the sources above the stated PhotonFlux.t completeness limit are “tentative” detections (defined by $0.003 < \text{ProbNoSrc_min} < 0.01$ in Table 1). Thus, that completeness limit may be somewhat optimistic. All other complete samples in that table contain $< 3\%$ tentative sources.

6.2. Spurious Sources

Our detection process is intentionally aggressive, and thus some weak spurious sources should be expected. The ultimate strategy for quantifying spurious detections is perhaps Monte Carlo simulation of the detection process executed on synthetic data sets that match the actual observations as closely as possible. Such simulations require an estimate of the spatially-variable background in the observations, which is problematic because by definition one must decide which photons come from point sources in order to identify which photons are “background”. Such simulations must also include artificial point sources because presumably one of the mechanisms for producing a spurious candidate in our detection procedure (Section 2) is imperfect image reconstruction in the wings of bright point sources. **Such simulations are infeasible due to the complexity of the Carina survey and the complexity of our detection procedures. Even if they could be performed, the result of such simulations—a characterization of the spurious source population in the full CCCP catalog—would be of little practical use because science analyses invariably involve additional sample selections of various kinds (e.g., matching to counterpart catalogs, source classification, selection within a region of interest on the sky). Propagating simulated spurious sources through sample selection and into science analysis would be a very difficult task.**

Perhaps the best method for gauging whether spurious sources may impact a scientific conclusion is to repeat the relevant science analysis on a smaller source sample obtained by applying a stricter criterion for source existence, e.g., by applying a smaller threshold on the ProbNoSrc_min (Table 1) statistic that was used to define the CCCP catalog (Section 2). Often, other criteria that define the source sample under study (e.g., involving counterparts, source classification, completeness cuts) have already removed most sources whose existence is uncertain. For example, in Section 6.1 we found that “tentative” detections are virtually absent from samples that are constructed to be complete in apparent photon flux.

Although we do not have an accurate estimate for the number of spurious sources in the CCCP catalog, a reasonable *upper limit* for that quantity is the number of X-ray sources for which no *true counterpart* exists in the deep HAWK-I infrared catalog, defined as the “unassociated X-ray population” in Section 5. Recall that the size of the unassociated population and the size of its complement, the “associated population”, are conceptually distinct from the number of X-ray sources without or with identified *matches*; the unassociated/associated fractions are estimated via detailed Monte Carlo simulations.

The size of the unassociated population is an upper limit, rather than a fair estimate, on the number of spurious X-ray detections because not every legitimate X-ray source is expected to be detected by HAWK-I. For example, the ~ 700 extragalactic X-ray sources in the HAWK-I field of view expected to be detected by the CCCP should be very faint in the near infrared (Getman et al. 2011); many will be below the completeness limits of HAWK-I ($J \sim 21$, $H \sim 20$, $K \sim 19$, Preibisch et al. 2011).

We have estimated the sizes of the unassociated and associated populations, with respect to HAWK-I, for the full CCCP catalog and for several smaller hypothetical X-ray catalogs (within the HAWK-I field of view) obtained by adopting more conservative requirements on source significance (smaller values of the ProbNoSrc_min statistic described in Section 2). Figure 9 shows that the size of the associated population (dark gray bars), which is assumed here to be a lower limit on the size of the legitimate X-ray detections, grows as we accept less and less certain X-ray detections. At the ProbNoSrc_min threshold we chose for the CCCP catalog (0.01), the associated population appears to still be growing. The cost of pushing deeper into the data is, of course, a rise in the number of spurious sources, assumed here to be bounded by the unassociated population (light gray bars).

There is no *correct* decision regarding the tradeoff between sensitivity and reliability. We generally take an aggressive approach to source detection for a variety of reasons. From a near term perspective, for studies of diffuse emission we feel that the added contamination arising from failing to identify and mask actual point sources is more damaging than the observing area lost to masking spurious point source detections. From a long term perspective, we are painfully aware that multiple decades may pass before this target is observed again by an X-ray observatory with an angular resolution superior to *Chandra*. We believe that recording tentative X-ray detections in the literature *may* prove valuable to future investigators, who will perhaps have access to observations in other bands that are far superior to what is currently available.

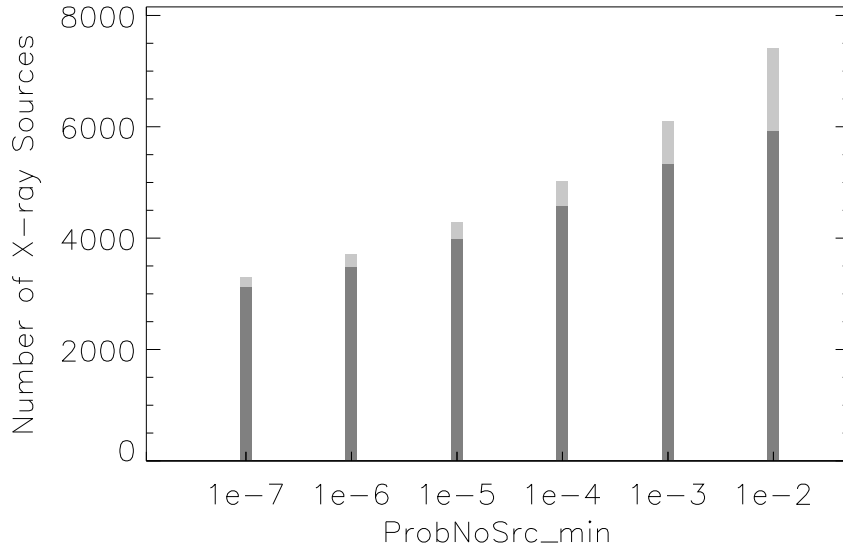


Fig. 9.— Estimated size of the associated (dark gray) and unassociated (light gray) components of hypothetical CCCP catalogs (within the HAWK-I field of view) defined by various thresholds on source significance (the ProbNoSrc_min statistic in Section 2).

A careful analysis of the 38 ACIS-I observations (totaling 1.2 Ms) that comprise the *Chandra* Carina Complex Project (CCCP) identifies and extracts 14,369 X-ray point sources; their positions and basic X-ray properties are presented in an electronic table. The catalog appears to be complete across most of the field to a limit of ~ 20 net X-ray counts (**corresponding to an absorption-corrected total-band luminosity of $\sim 10^{30.7}$ erg s $^{-1}$ for a typical low-mass pre-main sequence star**). Near the centers of the ACIS pointings, where the *Chandra* PSF is optimized, the completeness limit improves to ~ 6 net counts (**corresponding to an absorption-corrected total-band luminosity of $\sim 10^{29.9}$ erg s $^{-1}$ for a typical low-mass pre-main sequence star**). A large fraction of the detected sources lies beyond these completeness limits, e.g., more than half produced less than 10 net X-ray counts.

Forty sources have high-quality X-ray spectra (more than 500 net counts); most are known (Gagné et al. 2011; Nazé et al. 2011; Parkin et al. 2011; Townsley et al. 2011a) or candidate (Evans et al. 2011; Povich et al. 2011a) massive stars. Five suffer from mild photon pile-up in the detector; a new method for pile-up correction is described in Appendix A.

Counterparts to the majority (69%) of the X-ray sources are identified in a variety of visual and infrared catalogs, including newly-available wide-field and deep surveys in the near-IR (HAWK-I on the VLT) and mid-IR (*Spitzer*) bands. Most ($>80\%$) of the X-ray/counterpart source separations are $<1''$; the reliability of the counterpart identifications is discussed.

The X-ray catalog and counterpart identifications presented here provide the basis for later studies of the young stellar population in the Carina complex. Removal of the events associated with these sources allows study of the diffuse emission in this starburst region (Townsley et al. 2011b).

A. CHANDRA CCD PILE-UP RECONSTRUCTION

As outlined in Section 3, a few CCCP sources are sufficiently strong X-ray emitters to suffer from *photon pile-up*¹⁸—the arrival of multiple X-ray photons with a separation in time and space that is too small to allow each to be detected as a separate X-ray event. This phenomenon is ubiquitous among CCD-type detectors in X-ray astronomy and prevents standard analysis of source flux, variability, and spectrum (Allen et al. 1998; Bautz et al. 2000).

Various treatments of pile-up for the *Chandra* ACIS instrument have been proposed. Broos et al. (1998) and surely other authors point out that pile-up effects in point source spectra can be reduced by simply discarding events in the core of the observatory point spread function, where the incident photon flux is highest, and then applying appropriate energy-dependent calibration corrections to account for the discarded collecting area. *AE* supports this approach;¹⁹ for example, Getman et al. (2005) perform annular extractions for dozens of piled sources in the Orion Nebula Cluster.

The most commonly used pile-up analysis technique involves including pile-up effects in the observatory model employed by “forward fitting” spectral analysis packages such as *Sherpa* and *XSPEC*. These tools hypothesize an astrophysical model of the X-ray source, predict the instrumental spectrum that should be observed by employing observatory calibration information, compare the predicted and observed spectra, and adjust parameters of the astrophysical model to improve the prediction. Chartas et al. (2000) describe the derivation of astrophysical models for piled sources, using *XSPEC* to implement an astrophysical model and using a CCD simulator (Townsley et al. 2002a) to model the response of ACIS, including pile-up effects. Davis (2001) modeled pile-up with a parametrized integral equation, based on work by Ballet (1999). This model, which we will hereafter refer to as the “Davis model”, has been implemented in all the spectral analysis packages in common use by ACIS observers, and has been the sole technique applied to most piled ACIS sources for the past decade. Bayesian statistical methods have also been studied (Yu et al. 2000a,b; Kang et al. 2003; Yu et al. 2004), but are not in common usage among observers.

¹⁸http://cxc.harvard.edu/ciao/why/pileup_intro.html

¹⁹http://www.astro.psu.edu/xray/docs/TARA/ae_users_guide/pileup.txt

A.1. A New Forward-Fitting Algorithm

Figure 10 outlines a new variant to the forward modeling approach. Here a non-physical model of the source spectrum with many free parameters feeds an incident photon spectrum to the *MARX* mirror simulator²⁰, which produces simulated photons by modeling the *Chandra*-ACIS PSF and the observatory dither pattern²¹. A model of the ACIS CCD (Townsley et al. 2000, 2002a,b)²² simulates (1) the physical interaction of those photons with the CCD, (2) the process of reading out charge from the CCD (including charge transfer inefficiency²³ effects), (3) the process of detecting and grading²⁴ X-ray events, (4) the event list cleaning process that is applied to actual ACIS data, (5) assignment of event positions on the sky to remove the effects of the observatory’s dithered pointing, and (6) the extraction of events within the aperture chosen by the observer. Since the simulated photons have random arrival times, photon pile-up occurs naturally within the simulation in the form of superposition of electron charge clouds within individual CCD frames. The non-physical spectral model is iteratively adjusted until the piled simulated spectrum is similar to the observed spectrum, both in shape and in overall count rate. When an observed piled-up spectrum is reproduced in a satisfactory manner, the simulation is run one final time with pile-up disabled, by allowing only a single photon to arrive in each CCD frame. The reconstruction process thus produces two sets of simulated events derived from the same set of incident photons; the first exhibits pile-up due to Poisson arrival of the photons and resembles the observed spectrum, while the second is free from pile-up.

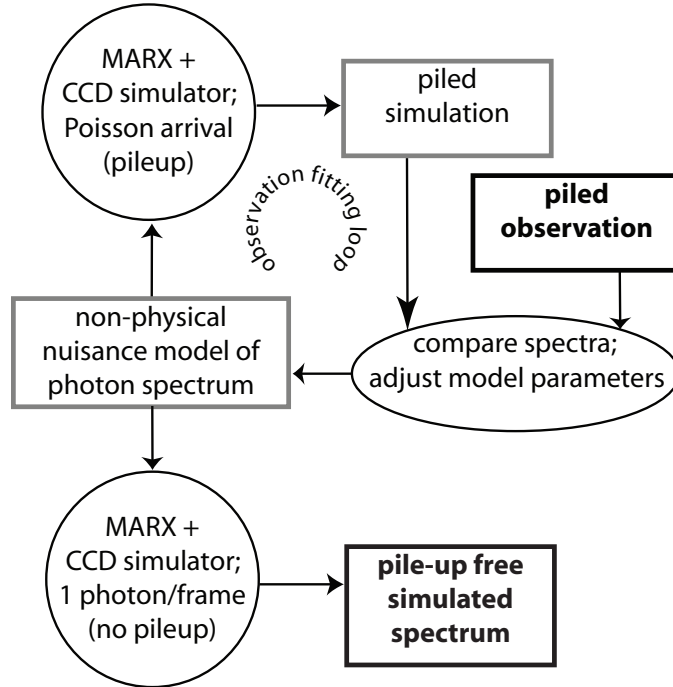


Fig. 10.— Data flow diagram for reconstructing a pile-up-free ACIS spectrum (bottom right) from a piled observed ACIS spectrum (top right). No interpretation is attempted on the non-physical model of an incident photon spectrum that reproduces the piled observation.

In principle, an *astrophysical* spectral model could be used in this fitting process, and then directly interpreted scientifically, without a need to simulate an ACIS spectrum free from pile-up. In such a scheme, the simulator would replace the response files that a fitting package like *XSPEC* uses to model the detector. However, our CCD simulator is not calibrated to reproduce the response of ACIS perfectly (e.g., time- and spatial variation of the ACIS optical blocking filter transmission,

²⁰<http://space.mit.edu/cxc/marx/>

²¹ During an observation, *Chandra* executes a slow pattern of motion around the nominal target coordinates known as dither (<http://cxc.harvard.edu/ciao/why/dither.html>).

²²Townsley et al. (2002a) and Townsley et al. (2002b) are available in the Physics database of ADS.

²³<http://cxc.harvard.edu/ciao/why/cti.html>

²⁴<http://cxc.harvard.edu/ciao/dictionary/grade.html>

time-varying charge transfer inefficiency, time-varying amplifier gains). Thus, we choose to fit a non-physical spectral model, then simulate an ACIS spectrum free from pile-up, and then fit that spectrum to astrophysical models in the normal way. We assume that small imperfections in the calibration of the simulation simply distort the input non-physical spectral model, leaving the pile-up phenomenon (superposition of photon charge clouds) in the simulation largely unperturbed. Thus, we expect that the simulated pile-up free event list is similar to what ACIS itself would have produced if pile-up were not present.

The observed (piled) spectrum is grouped (e.g., so that each group has a SNR of ~ 5) and the non-physical spectral model is parameterized by an independent photon flux for the energy range covered by each group. Within each iteration of the fitting process, the difference between the simulated and observed spectrum in each group is used to revise the corresponding photon flux parameter. This process is analogous to Lucy-Richardson image reconstruction; the redistribution of X-ray photon energy to observed event energy corresponds to the PSF of a telescope blurring the sky onto an observed image. The very flexible, non-physical model of the input photon spectrum we employ corresponds to the very flexible, non-physical model of the sky employed by Lucy-Richardson image reconstruction, which involves a free parameter for every pixel in the image. In both situations, the resolution of the model (size of the spectral group, or image pixel size) is usually smaller than the resolution of the instrument (energy resolution of ACIS, or PSF of a telescope). In both cases, Poisson noise will add features to the observation (spectrum or image) that are narrower than the energy resolution of the instrument, and thus cannot be reproduced by the model. This noise will tend to be amplified in the model (appearing as “salt-and-pepper” pixels in reconstructed images), as it strives to reproduce the noisy observation. However, the noisy photon flux model we derive is not interpreted in any way. It merely feeds a final pile-up free simulation, in which the noise in the model cannot produce features in the simulated spectrum that are any sharper or larger than the Poisson noise in the observation that sculpted the model.

The Davis model makes no use of any explicit information about the aperture that was used to extract X-ray events from the observation of a point source; indeed, that model can be used with diffuse sources. The original description of the model (Davis 2001) suggests a very generous point source aperture, and we are not aware of other documents that discuss the use of non-standard apertures. One of the attractive features of the pile-up reconstruction method outlined here is significant flexibility when choosing an extraction aperture. For example, this method can be applied to a piled source in a crowded region extracted with a reduced aperture to avoid a neighbor, as is done for two sources in Table 4. A non-standard aperture can be particularly helpful when a source suffers from severe pile-up, when the correlation between observed event rate and incident photon rate weakens or even becomes negative.²⁵ Use of an annular aperture in such a case discards the severely piled core of the PSF, restoring a positive correlation between observed event rate and incident photon rate, which this method requires in order to derive a model for the incident photon spectrum.

A.2. Application to Carina Sources

Detailed characterization of the performance of this spectral reconstruction technique will be performed in future studies. Ideally, analyses of piled observations would be judged against pile-up-free reference observations, using more appropriate targets that do not suffer the time variability expected for the massive stars exhibiting pile-up in the CCCP. In this study, we can roughly judge the reasonableness of the spectral reconstruction method by comparing its results to those obtained by the standard pile-up analysis technique, the “Davis model” described above.

For this comparison we choose the two most piled Carina sources from Table 4 that have the large extraction apertures required for the Davis model: WR 25 and QZ Car. We assess the consistency between the methods by simultaneously fitting the piled and reconstructed spectra in *XSPEC* (Arnaud 1996) to a single astrophysical model, and then examining the residuals of the fit. The *XSPEC* model for the piled spectrum includes a Davis model component to account for pile-up.²⁶

²⁵ See Figure 3 in the The *Chandra* ABC Guide to Pileup (http://cxc.harvard.edu/ciao/download/doc/pileup_abc.pdf).

²⁶ More precisely, *XSPEC* compares each of the two spectra to separate instances of a Davis+astrophysical model. The astrophysical

Figure 11 shows the resulting piled (red) and pile-up corrected (black) spectra, best fit models, and fit residuals. The standard effects of pile-up are seen in the relationship between the corrected and piled spectra: pile-up has reduced the overall count rate, but has hardened the spectrum by creating spurious events at high energy by combining two or more low energy photons. The most important aspect of these spectra, however, are their model residuals. The magnitude of the residuals for the reconstructed spectra and their similarity to the residuals for the piled spectra demonstrate the fidelity of the method introduced here, and provide additional confirmation of the Davis model.

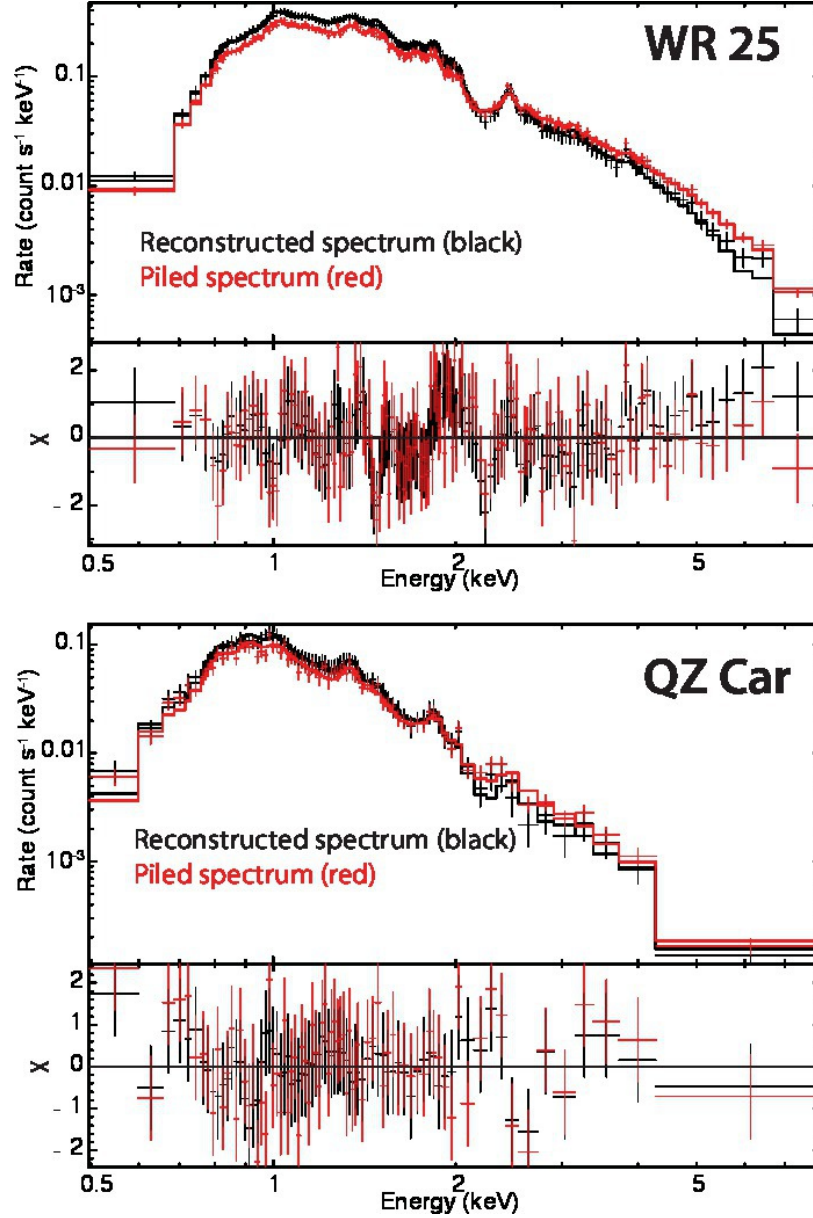


Fig. 11.— Observed (red) piled spectra and pile-up corrected (black) spectra of the Carina stars WR 25 (top) and QZ Car (bottom). The piled and corrected spectra are fit to a common astrophysical model, using the Davis model to account for pile-up in the former. Observed spectra are shown as data points with error bars in the upper sub-panels; models are shown as histograms; fit residuals are shown in the lower sub-panels.

Acknowledgments: We appreciate the time and useful suggestions contributed by our anonymous referee. This

parameters of the two model instances are tied together. The Davis model component for the reconstructed spectrum is effectively disabled by setting the frame time parameter to a very small value, and freezing all model parameters. The independent Davis model component for the piled spectrum allows the *alpha* and *psfrac* parameters to vary, and sets the frame time parameter to the value that appropriately accounts for the “FRACEXPO” effect, as described in the The *Chandra* ABC Guide to Pileup (http://cxc.harvard.edu/ciao/download/doc/pileup_abc.pdf).

work is supported by Chandra X-ray Observatory grant GO8-9131X (PI: L. Townsley) and by the ACIS Instrument Team contract SV4-74018 (PI: G. Garmire), issued by the *Chandra* X-ray Center, which is operated by the Smithsonian Astrophysical Observatory for and on behalf of NASA under contract NAS8-03060. This publication makes use of data products from the Two Micron All Sky Survey, which is a joint project of the University of Massachusetts and the Infrared Processing and Analysis Center/California Institute of Technology, funded by the National Aeronautics and Space Administration and the National Science Foundation. This work is based in part on observations made with the *Spitzer Space Telescope*, which is operated by the Jet Propulsion Laboratory, California Institute of Technology under a contract with NASA.

Facilities: CXO (ACIS), Spitzer (IRAC), VLT:Yepun (HAWK-I), CTIO:2MASS ()

REFERENCES

- Albacete-Colombo, J. F., Damiani, F., Micela, G., Sciortino, S., & Harnden, F. R., Jr. 2008, *A&A*, 490, 1055
- Allen, C. L., Plucinsky, P. P., McNamara, B. R., Edgar, R. J., Schulz, N. S., & Woo, J. W. 1998, *Proc. SPIE*, 3444, 198
- Anders, E., & Grevesse, N. 1989, *Geochim. Cosmochim. Acta*, 53, 197
- Arnaud, K. A. 1996, *Astronomical Data Analysis Software & Systems V* (ASP Conf. Ser. 101), ed. G. H. Jacoby & J. Barnes (San Francisco, CA: ASP), 17
- Ascenso, J., Alves, J., Vicente, S., & Lago, M. T. V. T. 2007, *A&A*, 476, 199
- Ballet, J. 1999, *A&AS*, 135, 371
- Bautz, M. W., et al. 2000, *Proc. SPIE*, 4012, 53
- Broos, P. S., Townsley, L. K., & Nousek, J. A. 1998, *Proc. SPIE*, 3444, 30
- Broos, P. S., Feigelson, E. D., Townsley, L. K., Getman, K. V., Wang, J., Garmire, G. P., Jiang, Z., & Tsuboi, Y. 2007, *ApJS*, 169, 353
- Broos, P. S., Townsley, L. K., Feigelson, E. D., Getman, K. V., Bauer, F. E., & Garmire, G. P. 2010, *ApJ*, 714, 1582
- Broos, P. S., et al. 2011, *ApJS*, submitted (CCCP Classifier Paper)
- Carraro, G., & Patat, F. 2001, *A&A*, 379, 136
- Chartas, G., et al. 2000, *ApJ*, 542, 655
- Cudworth, K. M., Martin, S. C., & Degioia-Eastwood, K. 1993, *AJ*, 105, 1822
- Cutri, R. M., et al. 2003, *The IRSA 2MASS All-Sky Point Source Catalog*, NASA/IPAC Infrared Science Archive
- Davis, J. E. 2001, *ApJ*, 562, 575
- DeGioia-Eastwood, K., Throop, H., Walker, G., & Cudworth, K. M. 2001, *ApJ*, 549, 578
- Delgado, A. J., Alfaro, E. J., & Yun, J. L. 2007, *A&A*, 467, 1397
- Evans, N. R., et al. 2011, *ApJS*, submitted (CCCP Tr16 B Stars Paper)
- Feigelson, E. D., Martin, A. L., McNeill, C. J., Broos, P. S., & Garmire, G. P. 2009, *AJ*, 138, 227
- Feigelson, E. D., et al. 2011, *ApJS*, submitted (CCCP Clustering Paper)
- Freeman, P. E., Kashyap, V., Rosner, R., & Lamb, D. Q. 2002, *ApJS*, 138, 185
- Fruscione, A., et al. 2006, *Proc. SPIE*, 6270
- Gagné, M., et al. 2011, *ApJS*, submitted (CCCP Massive Star Signatures Paper)

- Garmire, G. P., Bautz, M. W., Ford, P. G., Nousek, J. A., & Ricker, G. R., Jr. 2003, *Proc. SPIE*, 4851, 28
- Georgakakis, A., Nandra, K., Laird, E. S., Aird, J., & Trichas, M. 2008, *MNRAS*, 388, 1205
- Getman, K. V., et al. 2011, *ApJS*, submitted (CCCP Contaminants Paper)
- Getman, K. V., Feigelson, E. D., Broos, P. S., Townsley, L. K., & Garmire, G. P. 2010, *ApJ*, 708, 1760
- Getman, K. V., et al. 2005, *ApJS*, 160, 319
- Güdel, M., et al. 2007, *A&A*, 468, 353
- Hamaguchi, K., et al. 2009, *ApJ*, 695, L4
- Chandra Carina Survey HAWK-I paper, TBD
- Joye, W. A., & Mandel, E. 2003, *Astronomical Data Analysis Software and Systems XII*, 295, 489
- Kang, H., van Dyk, D. A., Yu, Y., Siemiginowska, A., Connors, A., & Kashyap, V. L. 2003, in *Statistical Challenges in Astronomy* (E.D. Feigelson & G. J. Babu, eds.), 449
- Kharchenko, N. V., & Roeser, S. 2009, *VizieR Online Data Catalog*, 1280, 0
- Kim, M., et al. 2007, *ApJS*, 169, 401
- Kissler-Patig, M., et al. 2008, *A&A*, 491, 941
- Lucy, L. B. 1974, *AJ*, 79, 745
- Luo, B., et al. 2008, *ApJS*, 179, 19
- Maschberger, T., & Kroupa, P. 2009, *MNRAS*, 395, 931
- Massey, P., & Johnson, J. 1993, *AJ*, 105, 980
- Massey, P., DeGioia-Eastwood, K., & Waterhouse, E. 2001, *AJ*, 121, 1050
- Monet, D. G., et al. 2003, *AJ*, 125, 984
- Muno, M. P., et al. 2009, *ApJS*, 181, 110
- Nazé, Y., et al. 2011, *ApJS*, submitted (CCCP Massive Star Lx/Lbol Paper)
- Ochsenbein, F., Bauer, P., & Marcout, J. 2000, *A&AS*, 143, 23
- Parkin, E. R., et al. 2011, *ApJS*, submitted (CCCP QZ Car Paper)
- Povich, M. S., et al. 2011, *ApJS*, submitted (CCCP Massive Star Candidates Paper)
- Povich, M. S., et al. 2011, *ApJS*, submitted (CCCP IR YSOs Paper)
- Preibisch, T., et al. 2011, *ApJS*, submitted (CCCP HAWK-I Paper)
- Puccetti, S., et al. 2009, *ApJS*, 185, 586
- Roeser, S., Demleitner, M., & Schilbach, E. 2010, *AJ*, 139, 2440
- Sana, H., Momany, Y., Gieles, M., Carraro, G., Beletsky, Y., Ivanov, V. D., de Silva, G., & James, G. 2010, *A&A*, 515, A26
- Siebert, A., & the RAVE collaboration 2008, *Astronomische Nachrichten*, 329, 892
- Skiff, B. A. 2009, *VizieR Online Data Catalog*, 1, 2023
- Smith, N., et al. 2010, *MNRAS*, 406, 952
- Townsley, L. K., Broos, P. S., Garmire, G. P., & Nousek, J. A. 2000, *ApJ*, 534, L139

- Townsley, L. K., Broos, P. S., Chartas, G., Moskalenko, E., Nousek, J. A., & Pavlov, G. G. 2002, *Nuclear Instruments and Methods in Physics Research A*, 486, 716
- Townsley, L. K., Broos, P. S., Nousek, J. A., & Garmire, G. P. 2002, *Nuclear Instruments and Methods in Physics Research A*, 486, 751
- Townsley, L. K., et al. 2011, *ApJS*, submitted (CCCP Intro Paper)
- Townsley, L. K., et al. 2011, *ApJS*, submitted (CCCP Diffuse Paper)
- Urban, S. E., Zacharias, N., Wycoff, O. G., & Washington, D. D. C. 2004, *VizieR Online Data Catalog*, 1294, 0
- Wang, J., et al. 2011, *ApJS*, submitted (CCCP Tr15 Paper)
- Wilms, J., Allen, A., & McCray, R. 2000, *ApJ*, 542, 914
- Wolk, S. J., et al. 2011, *ApJS*, submitted (CCCP Tr16 Paper)
- Yu, Y., Protassov, R., Surlas, E., & van Dyk, D. 2000, *Bulletin of the American Astronomical Society*, 32, 1207
- Yu, Y., van Dyk, D., Connors, A., Kashyap, V. L., & Siemiginowska, A. 2000, *Bulletin of the American Astronomical Society*, 32, 1431
- Yu, Y., Van Dyk, D., Siemiginowska, A., Freeman, P., Zezas, A., Kashyap, V., & Connors, A. 2004, *Bulletin of the American Astronomical Society*, 36, 935
- Zacharias, N., et al. 2010, *AJ*, 139, 2184
- Zacharias, N., Urban, S. E., Zacharias, M. I., Wycoff, G. L., Hall, D. M., Monet, D. G., & Rafferty, T. J. 2004, *AJ*, 127, 3043